



Characterising the occurrence of monomodal and multimodal ice hydrometeor populations and their fall speeds in midlatitude frontal ice clouds using radar Doppler spectra

Rosie M. Mammatt¹, Chris Westbrook¹, and Karina McCusker¹

¹Department of Meteorology, University of Reading, Reading, UK

Correspondence: Rosie M. Mammatt (r.m.mammatt@pgr.reading.ac.uk)

Abstract. Multimodality in vertically pointing radar Doppler spectra is frequently observed in stratiform clouds, but understanding the microphysical processes causing these signatures remains a challenge. In this study, we utilise Ka-band radar Doppler spectra from 23 deep stratiform clouds observed over Chilbolton, UK. We apply a peak finding algorithm to identify spectral reflectivity peaks in the Doppler spectra, which can be used to infer the presence of distinct coexisting ice particle populations, such as pristine crystals mixed with aggregate snowflakes. Using these results, we can provide the first quantitative estimate for the distribution of multimodal spectra with temperature. There are two clear temperature regimes where the occurrence of multimodal spectra increases sharply, indicating production of new particles; these are between -8°C and -3°C , which we attribute to rime splintering, and between -18°C and -13°C , where the mechanism responsible for producing multimodal spectra is unclear.

The peak finding algorithm also returns the velocities associated with the peaks in spectral reflectivity, which allows us to analyse the distribution of velocity with temperature for primary and secondary particle populations. We show evidence that primary populations from monomodal spectra experience a significant reduction in fall velocity at -13°C . We show evidence that this feature is governed by the primary population; that is, falling particles are slowing down. Dendritic growth is favoured near this temperature, and we therefore hypothesise that particles such as polycrystals and aggregates, which form in colder cloud layers, precipitate to this level, form dendritic branches, and therefore experience increased air resistance.

1 Introduction

Although only a small fraction of global precipitation reaches the surface as snow, satellite observations have provided evidence that the majority of precipitation events originate from the ice phase (Field and Heymsfield, 2015; Heymsfield et al., 2020). Ice microphysical processes also have a significant influence on radiative balance due to the interaction of ice crystals with solar radiation; studies have suggested that changing particle habits, phase and size distributions are likely to have noticeable climate impacts (Hofer et al., 2019; Zhang et al., 2022; Pasquier et al., 2023). Uncertainties in how ice microphysical processes will change in both ice and mixed phase clouds are responsible for some of the greatest uncertainties in future climate predictions (Sun and Shine, 1994; Lohmann and Feichter, 2005; Sherwood et al., 2020; Mülmenstädt et al., 2021). This motivates continual improvement in our understanding of ice microphysical processes and their representation in both numerical weather prediction



25 (NWP) and climate models. Interpreting remote sensing observations is also dependent on our fundamental understanding of ice microphysical processes and characteristics.

Accurate representation of ice particle size distributions (PSDs) remains a challenge. Mammatt et al. (2026) use aircraft observations to evaluate the accuracy of the double moment gamma parameterisation from the Cloud and AeroSol Interacting Microphysics (CASIM) scheme (Field et al., 2023), which has recently been implemented in the operational UK Met Office Unified Model. Examination of the observed PSDs, particle images and particle shape analysis showed evidence that the PSD shape was influenced by secondary ice production (SIP), leading to a bimodal PSD. This led to poor representations of the observed PSDs as the parameterisation could not simultaneously fit the high concentration of relatively small particles produced by SIP as well as the lower concentration of relatively large particles. This resulted in large errors in forecast process rates, including underestimating aggregation rate by up to 50 % and precipitation rate by up to 25 %. The analysis in Mammatt et al. (2026) is based on one case study, but demonstrates the importance of accurately representing ice PSDs in NWP models and how multimodal populations can impact that representation. It is therefore desirable to look at a larger dataset to better understand how frequently and at what temperatures bimodal PSDs are observed. In the present study, this will be achieved by identifying spectral reflectivity peaks in vertically pointing radar Doppler spectra, from which the presence of multimodal PSDs can be inferred, along with the fall velocity of these populations. Gathering statistics over many events will allow us to quantify the occurrence of multimodal spectra and of the velocity of different particle populations with temperature. The aim is to contribute to improving interpretation of the microphysical processes active at different temperatures, which may be used to inform representations of ice microphysical processes in NWP models and analysis of remote sensing retrievals in the future.

Vertically pointing radar Doppler spectra provide information on particle vertical velocities with altitude. From these it is possible to identify coexisting particle populations that are distinguishable by their velocities (Kollias et al., 2002; Luke and Kollias, 2013; Kneifel et al., 2016). The terminal velocity of large unrimed snowflakes generated by aggregation is almost independent of particle size as the additional drag caused by the larger cross-sectional area opposes the effect of increasing mass (Kneifel and Moisseev, 2020). From in situ and radar observations, there is evidence to suggest that this terminal velocity is about 1 m s^{-1} , assuming surface pressure and negligible vertical air motion (Zawadzki et al., 2001). SIP produces high concentrations of very small particles, and these populations of secondary particles are distinguishable from the primary population due to their very slow vertical velocities (Shupe et al., 2004; Kalesse et al., 2016; Field et al., 2017). Riming, on the other hand, increases the vertical velocity of particles relative to an unrimed population due to their increased mass and fall characteristics (Zikmunda and Vali, 1972; Locatelli and Hobbs, 1974; Mosimann, 1995). It is therefore possible to segregate coexisting particle populations observed in Doppler spectra due to differing fall speeds, and to infer the microphysical processes resulting in differing velocities.

Ice multiplication influences the shape of observed Doppler spectra by forming populations of small particles with slow fall speeds. It has long been observed that concentrations of ice nucleating particles (INPs) can be many times lower than observed concentrations of ice crystals in clouds (Field et al., 2017), and SIP has therefore been a topic of interest for a number of years. Generally, however, studies have focussed on SIP in convective clouds, with relatively little attention paid to stratiform frontal clouds. Hallett and Mossop (1974) first showed evidence for the production of secondary ice particles that result from



60 the splintering of a liquid cloud droplet during the riming process. These splinters are initially very small but as they grow
in both size and mass, they appear as a secondary particle mode in radar Doppler spectra which is distinguishable from the
primary population by their slow fall velocity (Zawadzki et al., 2001). Hallett and Mossop (1974) suggest that rime splintering is
observed to be active in a relatively narrow temperature regime of approximately -3°C to -8°C . Since this first study, there have
been numerous studies further investigating this process using in situ aircraft observations (Crosier et al., 2011, 2014; Lloyd
65 et al., 2014; Keppas et al., 2017). However, results from recent laboratory studies suggest there are still discrepancies regarding
the efficiency of this mechanism (Seidel et al., 2024). Droplet fragmentation has also been investigated as a mechanism of
generating secondary particles (Phillips et al., 2018), which is thought to require drizzle drops of at least $50\mu\text{m}$ (Wildeman
et al., 2017) but may be more efficient for larger drops of more than $300\mu\text{m}$ (Lauber et al., 2018; Keinert et al., 2020). Ice-ice
collisional breakup has also been proposed as an efficient SIP mechanism (Vardiman, 1978; Yano and Phillips, 2011; Yano
70 et al., 2016; Phillips et al., 2017), in which ice fragments are produced during collisions between ice particles. Whilst there is
a lack of agreement surrounding the conditions in which the droplet fragmentation and ice-ice collisional breakup mechanisms
are active, there is evidence to suggest that they occur over a broader temperature range than rime splintering (Field et al.,
2017; Korolev and Leisner, 2020).

This study will be presented as follows: in Sect. 2, we describe the radar and model data used and explain the processing of
75 the spectral data. In Sect. 3, we explain the peak finding algorithm used to identify spectral reflectivity peaks in the Doppler
spectra and how the parameters for the algorithm were chosen and validated. We assess the turbulent contribution to the
spectral width and explain the impact this has on the accuracy on the peak finding algorithm, filtering out data which is
impacted. In Sect. 4, we apply the method to 23 case studies and use the results from the peak finding algorithm to quantify
how frequently multimodal spectra are observed in radar Doppler spectra as a function of temperature. We present evidence
80 that rime splintering causes the high percentage of observed multimodal spectra at -5°C , but also find evidence that production
of secondary particles is occurring in a second temperature window of -10°C to -18°C . The mechanism for this is unclear.
We then investigate the distributions with temperature of particle population velocity and mean Doppler velocity (MDV), and
how these differ between monomodal and multimodal microphysical regimes. To our knowledge, there are limited studies in
the existing literature quantifying the fraction of multimodal spectra with temperature in frontal clouds and which demonstrate
85 the impact of multimodal cloud regimes on Doppler radar measurements.

2 Data

2.1 Radar data

The Copernicus Ka-band (35 GHz) radar at the Chilbolton Facility for Atmospheric and Radio Research (CFARR) takes
continuous routine observations, including reflectivity, MDV, standard deviation of mean Doppler velocity (σ_v) and spectral
90 width (Walden, 2026). It also takes observations of Doppler spectra every minute. It has a range of 15 km with a 60 m range
resolution, and can measure particle vertical velocities between -10.72m s^{-1} and 10.72m s^{-1} (see Illingworth et al., 2007,
for instrument specifications and capabilities). Note that here and throughout this study, negative velocities indicate movement



towards the radar, and therefore indicate descending hydrometeors for our vertically pointing radar. Increases or decreases in velocity will be discussed in the absolute sense whilst retaining the negative sign convention. Using archived data, we identify 23 frontal case studies from a 14 month period in 2017-2018 to examine in closer detail; Table 1 provides further detail on each of these cases. They were selected to represent typical frontal clouds, and are primarily stratiform with large vertical extents which cover a wide range of temperatures, often with surface precipitation for part of the observation period. Comparison with archived surface pressure analysis charts from the UK Met Office provides confirmation that the clouds in the selected cases are associated with synoptic scale low pressure systems. Reflectivity, example spectrograms, and results from the peak finding method (see Sect 3.1) are shown for each case in the Supplement. Data are received in their raw, uncalibrated form, and therefore noise correction and calibration methods must be applied before further analysis is carried out. Corrections to reduce the impact of signal attenuation by rain and turbulent Doppler spectra broadening are also applied. These processes are explained in the following sections.

Table 1: Description of the case studies selected to examine in further detail in our analysis. Depth of system is estimated to within 0.5 km from examination of radar images, and refers to the depth above the melting layer. Cloud top temperatures are estimated to within 5 °C from comparison between radar images and model data (see Sect. 2.2). Multimodal occurrence refers to the percentage of all in-cloud pixels which are identified as multimodal. Maximum surface rain rates are those associated with the main deep frontal cloud observed on each day, and were measured with a high resolution rain gauge (Norbury and White, 1971) at CFARR. Descriptions of the synoptic situation are based on surface pressure analysis charts from the UK Met Office, and highlight the features that cloud is associated with.

Case study	Date	Depth of system (km)	Cloud top temperature (°C)	Multimodal occurrence (%)	Maximum rain rate (mm hr ⁻¹)	Synoptic situation
1	6 January 2017	7.0	-45	8.7	4.7	Warm front followed by two occluded fronts approaching from the north west
2	15 January 2017	6.0	-35	21.9	2.4	Slow moving warm front from the west
3	27 January 2017	7.5	-50	5.1	2.2	Multiple fronts approaching from the south west
4	29 January 2017	9.0	-40	19.3	12.5	Series of warm fronts from the south west
5	1 February 2017	9.0	-50	10.7	5.1	Cold front associated with a series of low pressure systems from the west
6	6 February 2017	8.0	-30	18.7	8.8	Upper level warm front associated with a very deep low pressure (~ 930 hPa) over the Atlantic Ocean



Case study	Date	Depth of system (km)	Cloud top temperature (°C)	Multimodal occurrence (%)	Maximum rain rate (mm hr ⁻¹)	Synoptic situation
7	1 March 2017	9.0	-50	15.4	1.9	Series of occluded fronts from the south west
8	3 March 2017	8.0	-50	7.8	27.4	Warm front followed later by a cold front from the same low pressure system from the south
9	12 March 2017	4.0	-25	12.6	7.1	Cold front from the west
10	22 March 2017	7.0	-40	14.0	11.0	Cold front associated by a nearby weak low pressure system
11	27 April 2017	3.0	-20	7.3	3.1	Warm front approaching from the north
12	17 May 2017	8.0	-50	13.7	14.0	Two cold fronts approaching from the west
13	27 June 2017	7.5	-45	7.1	7.8	Upper level cold front to the west
14	21 July 2017	7.0	-40	11.1	51.1	Cold front associated with a low pressure system located over Ireland
15	29 July 2017	7.0	-45	10.5	6.0	Warm front approaching from the south
16	9 August 2017	7.0	-40	13.7	12.0	Occluded front from the north west
17	3 September 2017	6.0	-35	16.9	6.4	Occluded front followed by a cold front approaching from the south west
18	17 October 2017	6.0	-35	10.8	12.4	Upper level front associated with a weak low pressure system to the south west of the UK
19	19 October 2017	6.5	-45	13.3	8.9	Series of cold fronts from the west
20	4 November 2017	8.0	-45	14.2	12.5	Multiple cold and occluded fronts from the west
21	10 December 2017	9.0	-50	17.8	8.2	Series of fronts associated with a low pressure system which passes west across the UK
22	30 December 2017	8.0	-25	23.9	3.8	Warm front from a low pressure system to the west of Ireland
23	14 February 2018 ^a	8.0	-35	17.8	6.5	Multiple fronts from a deep low pressure (~ 945 hPa) south of Iceland

^a Detailed analysis of aircraft data for this case can be found in Mammatt et al. (2026).



2.1.1 Noise correction

105 To extract the main spectral reflectivity peak and remove artefacts caused by echoes, we apply noise correction to the spectral data. This is achieved by estimating the mean background noise value, P_{noise} , by calculating the mean spectral power of empty gates; the standard deviation of the power in these empty gates is also calculated. P_{noise} is then subtracted from the remaining spectra and data within three standard deviations of P_{noise} are removed. This method allows us to retain the vast majority of the observed spectra, even at low reflectivities. This is important for providing information on the small, slow moving (and therefore weakly reflecting) ice particles. At this stage, the data are still in their uncalibrated form, so the next step is to apply a calibration. We also apply a range correction which accounts for the increased spread of the radar beamwidth with range, which is

$$Z_c = P_u + 20\log_{10}(R) - C_{\text{calibration}} \quad (1)$$

where Z_c is the calibrated reflectivity, P_u is the uncalibrated power of the signal, and $C_{\text{calibration}}$ is a calibration constant, all in dB units. R is the range in metres. The Copernicus radar is routinely calibrated by comparing the signal to that from the Chilbolton Advanced Meteorological Radar (CAMRa), which operates in the S-band and is absolutely calibrated to within ± 0.5 dB in Rayleigh scattering cirrus clouds.

Figure 1 shows an example of a noise-corrected spectrogram (stacked Doppler spectra with height); this example is from 17 May 2017. Figure 1a shows the full spectrogram, and we can see that the melting layer is very clear in this example. There is a sharp increase in the observed Doppler velocities and range of velocities at approximately 3 km, which is because rain falls significantly faster than ice particles (Field et al., 2005). The primary mode is falling at $\sim 0.7\text{--}1.5 \text{ m s}^{-1}$ and there are two regions at higher altitude where evidence for multimodality is visible, which can be seen in closer detail in Fig. 1b. At 3–4 km and 5–6 km, we see that there are two ‘strands’ to the spectrogram, which is indicative of a particle population which is evolving independently to the primary population.

125 2.1.2 Assessing the effect of turbulence on Doppler spectra

Due to the stratiform nature of the cases selected for this study, we expect that the primary influence on the observed Doppler spectra will be particle fall speeds. However, turbulence also acts to broaden the Doppler spectra (Babb et al., 2000). To assess the impact of air turbulence on the observed Doppler spectra examined, we follow the technique described in O’Connor et al. (2005) to quantify the contribution of turbulence to the width of our observed spectral peaks. The broadening of the Doppler spectrum due to homogeneous isotropic turbulence is

$$\sigma_t^2 = \sigma_v^2 \frac{L_s^{\frac{2}{3}}}{L_t^{\frac{2}{3}} - L_s^{\frac{2}{3}}}, \quad (2)$$

where σ_v^2 is the standard deviation of the mean Doppler velocity over a time window (in our case this time window is 30 s). L_s and L_t are the length scales for spectral and moment level observations respectively. The length scale L is calculated by

$$L = Ut + 2z \sin\left(\frac{\theta}{2}\right), \quad (3)$$

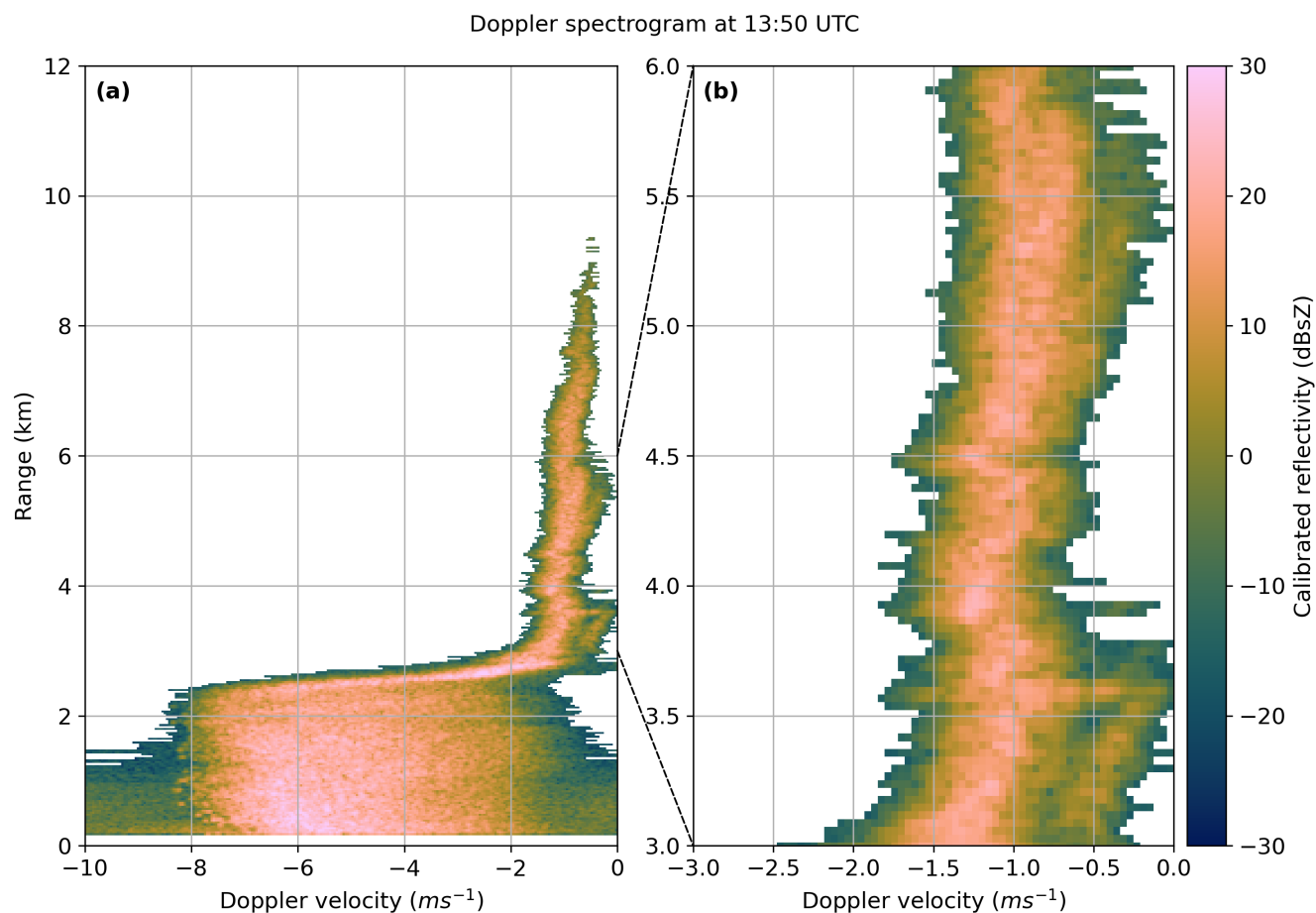


Figure 1. An example of the routine Doppler spectra observed at CFARR. This example is from 13:50 UTC on 17 May 2017. Negative velocity values indicate movement towards the radar. Panel (a) shows the full spectrogram and panel (b) shows a closer view of the ice phase regions of the spectrogram where multimodal spectra are present.

135 where $t=1$ s for L_s and $t=30$ s for L_t , corresponding to the sampling time of a single MDV estimate versus the window for computing $\sigma_{\bar{v}}$. U is the horizontal wind speed, z is the height in metres and θ is the beamwidth of the radar in radians (the Copernicus radar has a beamwidth of 0.25°).

Figure 2 shows an example of the quantities involved in these calculations. Figure 2a shows the standard deviation of mean Doppler velocity from the moment level observations. Figure 2b shows the magnitude of the horizontal wind speed, calculated from the zonal and meridional model winds (see Sect. 2.2). Figure 2c shows the turbulent contribution to spectral width, calculated using the method outlined above. In this example, we see that the turbulent contribution to the spectral width is generally very low throughout the majority of the cloud, with values generally below 0.05 m s^{-1} . There is a region at around 13:00 UTC where there is a significant increase in σ_t , with values in excess of 0.2 m s^{-1} . This provides evidence to suggest



145 that turbulent processes in this region of the cloud act to broaden of the observed Doppler spectra here. By examination of these results and comparisons with individual spectra, we choose a threshold of 0.042 m s^{-1} (equal to one velocity bin in our Doppler spectrum) and remove data where the turbulent contribution is greater than this threshold. Ice microphysical processes happen at low fall speeds so sensitivity to small velocity changes from external factors is high; this has impacts for further analysis, such as identifying individual populations and mechanisms. Our conservative velocity threshold removes these effects, whilst allowing the vast majority of data to be kept.

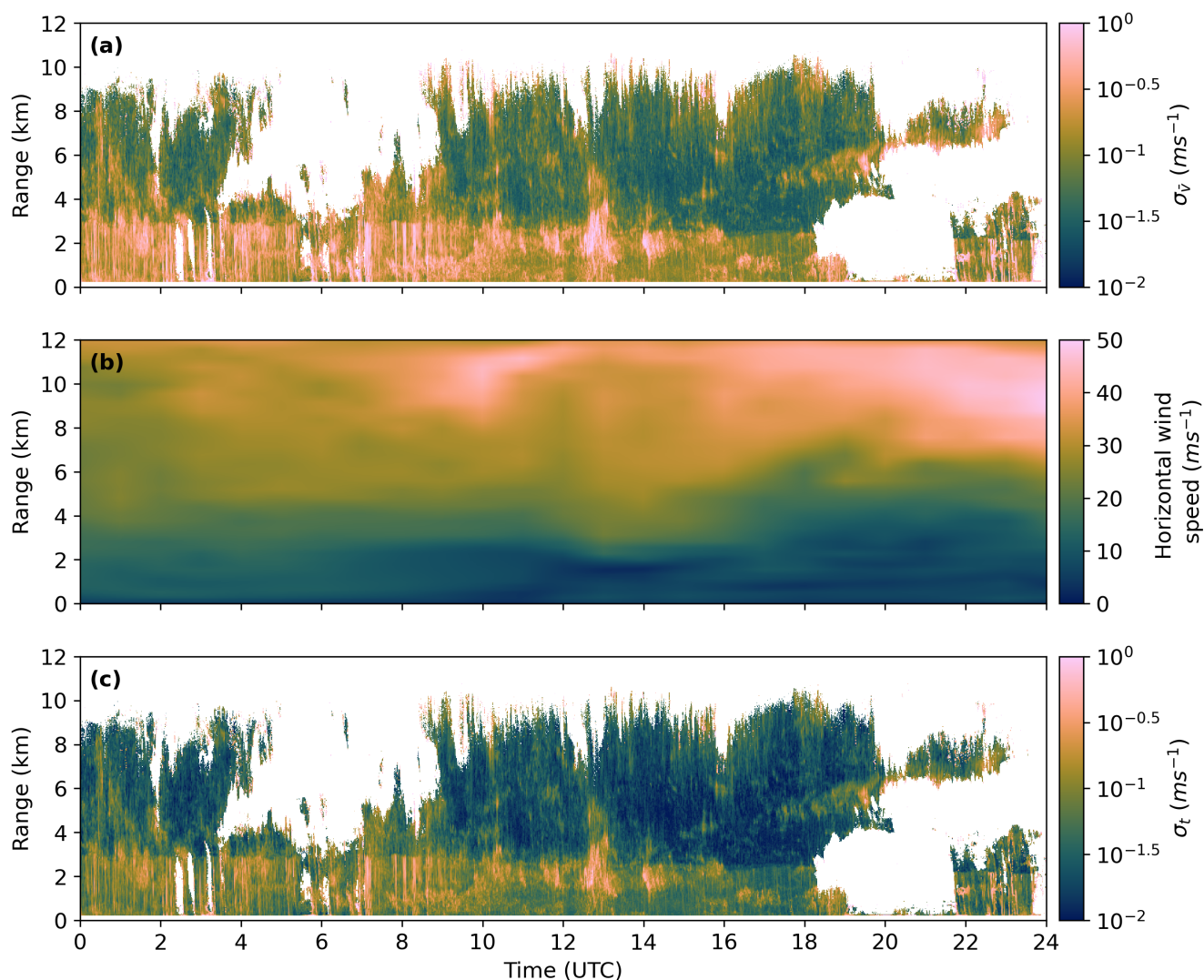


Figure 2. Panel (a) shows the standard deviation of mean Doppler velocity, σ_v , from the moment level observations. Panel (b) shows the magnitude of the horizontal wind speed from the model. Panel (c) shows the turbulent contribution to spectral width, σ_t , estimated using the method described in Sect. 2.1.2 for the cloud volume observed on 17 May 2017.

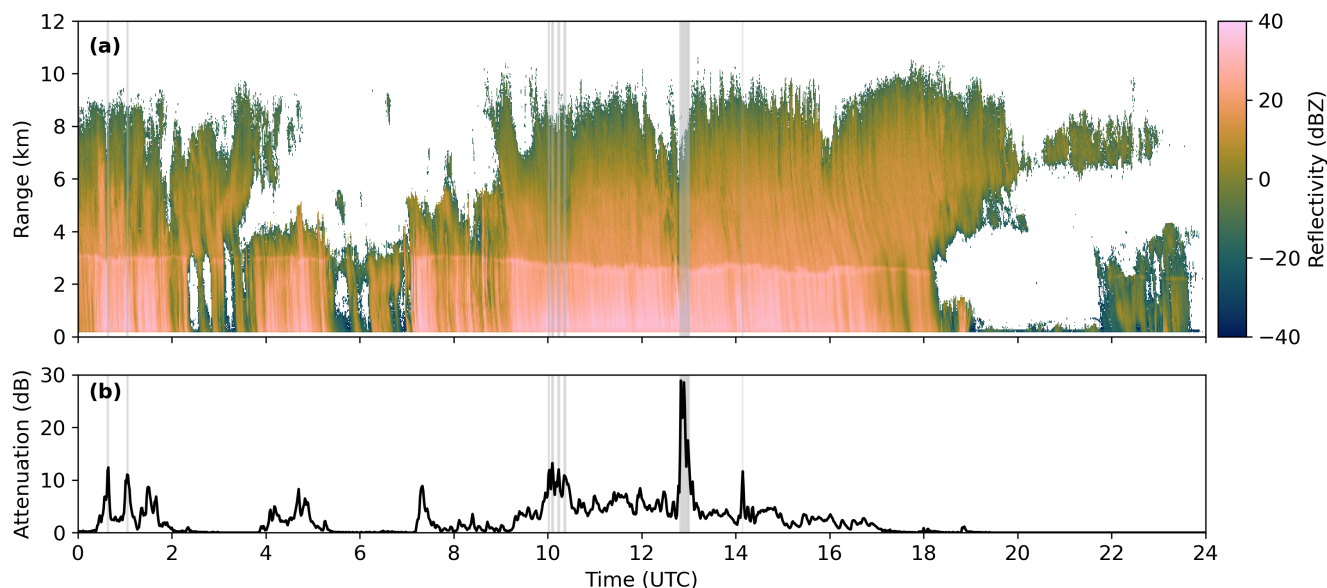


Figure 3. Radar image calculated from integrated Doppler spectra (a) and total attenuation (b) for the example case. The grey shading in both panels shows where attenuation exceeds 10 dB.

150 2.1.3 Impact of rain attenuation

Attenuation of radar signals by raindrops results in weakened echoes. The key results presented in the following sections are not sensitive to attenuation, as it does not influence the shape of the spectra but simply causes a reduction in the reflectivity across the whole spectrum. It is possible, however, that high levels of attenuation may cause spectral peaks with lower spectral reflectivities to fall below the noise floor and thus be removed; it is therefore desirable to identify and neglect regions which are heavily influenced by attenuation. Rain rate is measured at CFARR using a high resolution rain gauge (Norbury and White, 1971), and we can use this to estimate attenuation of the radar signal strength caused by rain. One-way attenuation for a Ka-band radar is given by

$$a \approx 0.28R \tag{4}$$

(Matrosov, 2005), where a is the attenuation (in dB km^{-1}) and R is the rain rate (in mm hr^{-1}). Using the 0°C isotherm from the model (see Sect 2.2), the total attenuation caused by rain below the melting layer is estimated. Figure 3a shows the radar image calculated from the integrated Doppler spectra, and Fig. 3b shows the total attenuation estimate. The grey shading in both panels shows where attenuation exceeds 10 dB. We can see that the peak of nearly 30 dB of attenuation seen at around 13:00 UTC corresponds to an apparent drop in cloud top height, to around 6 km from approximately 10 km at neighbouring times; we suggest that this reduced echo top is in fact a result of weakened signal rather than a physical feature. To remove the influence of events like this, we exclude regions of cloud where the attenuation estimate exceeds 10 dB.



2.2 Model data

Archived NWP model data for Chilbolton for each case was obtained via the ACTRIS Cloudnet portal. ICON model data (Zängl et al., 2015) is available for cases from 6 January to 17 May 2017, which has a lead time of 12–23 hours, and ECMWF IFS data (Wedi et al., 2015) is available for cases from 27 June 2017 to 14 February 2018, which has a lead time of 12–
170 35 hours. Variables are forecast hourly in both models. Here, we are primarily interested in temperature from the models so that comparisons can be made with the location of different microphysical features. Doppler spectra measurements are made every minute; we therefore interpolate the temperature field onto the same grid so that we have a temperature profile for every Doppler spectrogram. The horizontal wind fields are also used as inputs to equation 2.

3 Methods

175 3.1 Doppler spectra peak finding algorithm

In order to quantify the fraction of multimodal spectra in our case studies, we identify the number of peaks in the one dimensional Doppler spectra at each time and height gate (hereafter referred to as ‘pixels’). It is unrealistic to manually identify the spectral peaks in each of the 15.9 million pixels examined in this study, so we apply a peak finding algorithm to the one dimensional Doppler spectra. We use the SciPy function ‘find_peaks’ (Virtanen et al., 2020) to identify peaks in spectral reflectivity.
180 Section 3.1.1 and Table 2 describes these parameters in more detail and how they were chosen, and Sect. 3.1.2 describes how we validate the accuracy of the peak finding parameters.

3.1.1 Choosing peak finding parameters

The tuneable parameters and values chosen for the ‘find_peaks’ function are outlined in Table 2. Height determines the minimum spectral reflectivity at which a peak can be identified; the low threshold chosen here was purely to remove any remaining
185 noise that had not been removed during the noise correction process (described in Sect. 2.1.1). The method for finding the prominence of peaks is demonstrated using idealised spectra in Fig. 4. Prominence is found by extending a horizontal line in both directions from the top of a peak until it intersects with the slope of a higher peak or the edge of the spectrum, shown as the red dotted lines in Fig. 4. The difference between the lowest signal value between these two points and the height of the peak is the prominence, shown by the blue dashed line in this figure. Changing the prominence threshold changes the minimum
190 length of the blue line whilst still retaining this maximum as a distinct peak.

We remove peaks where the spectral reflectivity is more than 30 dB lower than the spectral reflectivity of the largest peak. This has little impact on the overall results, but helps remove artefacts identified on the very edge of the one dimensional spectra which arise from imperfections in radar hardware. There are several other optional parameters which are described briefly in Table 2, but we found no significant change in results when they were applied and were therefore not implemented
195 for simplicity.



Table 2. Description of the parameters from SciPy’s peak finding algorithm (Virtanen et al., 2020) and the values chosen. Parameters with a value of ‘None’ were not used in this method.

Parameter	Description	Value
Height	Minimum reflectivity at which a peak can be identified	-15 dBsZ
Prominence	Height of the peak relative to the height of the nearest valley	1dB
Distance	Distance between peaks	None
Width	Width of the peak at half its height	None
Window length	Window length in which parameters e.g. prominence are calculated	None
Threshold	Distance to the directly neighbouring samples	None
Plateau size	Required size of the flat top of peaks	None

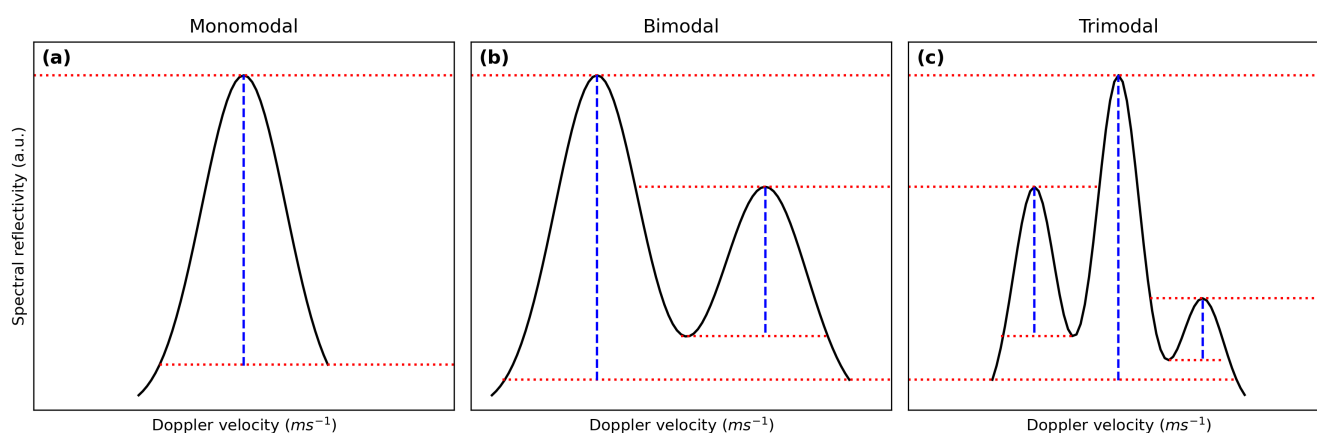


Figure 4. Idealised monomodal (a), bimodal (b), and trimodal (c) spectra. The red dotted lines show the identified minima and maxima of the spectra, and the blue dashed lines show the difference between these; this equates to the prominence. See text for a more comprehensive description. The y-axis shows spectral reflectivity in arbitrary units (a.u.) and the x-axis represents Doppler velocity.

The one dimensional Doppler spectra for each pixel are noisy in their raw form, where noise in this context refers to both of the effects of a sampling a finite number of independent realisations of the hydrometeor population and the influence of receiver noise. A moving average is therefore calculated for each spectra before the peak finding algorithm is applied. This prevents random variations in the spectral reflectivity profile being identified as peaks. Choosing the number of velocity bins (dV, each of width 0.042 m s^{-1}) to apply the moving average across is non-trivial; too short a window means not enough of the noise is smoothed out, whilst too long a window causes the peaks to lose magnitude and separation, and they therefore begin to merge into each other. It is also important to inspect whether the chosen averaging window works equally well on monomodal and multimodal spectra, as well as in cases where the velocity separation between coexisting populations is marginal. Figure 5 shows examples of the process by which this parameter was chosen. With the prominence threshold fixed at 1 dB, we increase the averaging window gradually and apply the peak finding algorithm to each smoothed spectra to show when the ‘true’ peaks



are being correctly identified without noise contamination, and when peaks start to be lost due to over-smoothing – this occurs when the prominence of a peak falls below the 1 dB threshold. Figure 5a shows an example of a marginal multimodal spectrum, where small changes in the peak finding methodology have the most influence over the classification of this spectrum. We see that an averaging window of at least two velocity bins is required to smooth the noise; this prevents identification of the narrow peak on the left tail of the distribution, which is unlikely to be caused by microphysical features. However, we see in this example that a small change in the averaging window of three to four velocity bins would make the difference between spectra like these being identified as trimodal or monomodal. Comparison with the full Doppler spectrogram shown in Fig. 1 provides insight into the microphysical properties at this height, and we see that it is likely that there are multiple collocated particle populations. Figure 5b shows an example of a monomodal spectrum, where we would expect only one particle population to be identified. The importance of choosing the correct averaging window is again apparent in this example, as it is clear that the noisy nature of the raw spectrum has a greater influence. Here, an averaging window of at least three velocity bins is required to effectively smooth out the noise. Figure 5c shows a bimodal spectrum of two particle populations with very distinct vertical velocities. We expect that cases such as these should be comparatively easy for the algorithm to accurately detect the peaks. Indeed it can be seen that the ‘true’ peaks are correctly identified with only a minimal averaging window of two velocity bins, and longer averaging windows do not change the results here. Taking these and many similar examples into account, we decide that an appropriate averaging window is three velocity bins (3 dV). This provides a good compromise between sufficient smoothing to reduce the impact of noise without reducing the signal of marginally differing populations in multimodal spectra.

A similar test can be performed to show the effect of varying the value of the prominence threshold whilst fixing the averaging window at three velocity bins, the results of which are presented in Fig. 6. We find the small changes of this prominence threshold have less of an influence on the results than changing the averaging window length. In row (a), we see that the prominence threshold must reach 1.4 dB before it starts to influence the number of peaks identified for this spectrum. We find in row (b) that a low threshold of less than 0.4 dB causes an extra peak to be identified here. Inspection of the spectrogram shown in Fig. 1 suggests that the particle population at this height is monomodal, so we would expect a single peak to be identified here. This suggests that the low reflectivity peak identified in these spectrum is a result of noise in the observed Doppler spectrum which the averaging process has not smoothed completely. Figure 6 shows that even a relatively low prominence threshold is sufficient to remove features such as this, which demonstrates the importance of utilising this parameter. Row (c) provides evidence that the prominence values tested here have no influence on the number of peaks detected for multimodal particle populations with peaks that are well separated in velocity and spectral reflectivity. Taking these and many such examples into account, we decide that a prominence threshold of 1 dB is sufficient to prevent ‘false’ peaks being identified, but is not high enough to prevent the detection of particle populations separated by small changes in velocity and spectral reflectivity. Having settled on the value of the prominence threshold independently, we find that it is in good agreement with the value used in previous studies which use machine learning techniques to identify peaks in one dimensional Doppler spectra (Radenz et al., 2019; Vogl et al., 2024).

Whilst this peak finding method is accurate in ice and mixed phase cloud regions, it has not been tested in liquid phase regions. However, we find that it is inaccurate in rain because it has a broad and noisy reflectivity spectrum. For this study, we

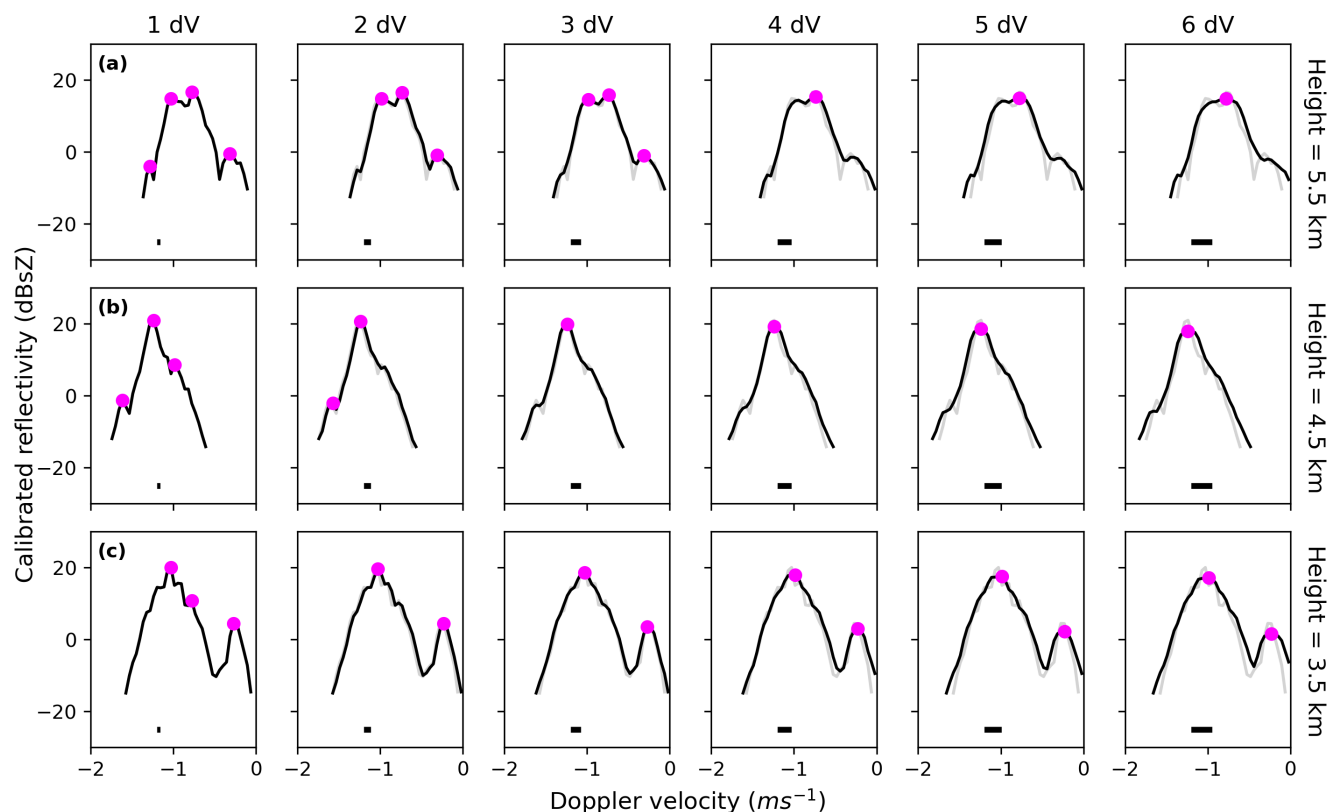


Figure 5. One dimensional Doppler spectra from heights of 5.5 km (a), 4.5 km (b) and 3.5 km (c) in the example shown in Fig. 1. The grey line in each panel shows the spectra with no smoothing, and the black line shows the smoothed spectra calculated using increasing averaging windows. The length of the averaging window is described by the number of velocity bins that the moving average is calculated across; dV is the velocity bin width, equal to 0.042 m s^{-1} . Note that the grey line is not visible when the averaging window is 1 dV as this equates to no smoothing. The thick black line at the bottom of each panel represents the width of the averaging window relative to the velocity scale. The peaks identified by the peak finding algorithm using the parameters described in Table 2 for each spectra are shown by the magenta points.

are interested in processes in the ice phase and can therefore apply a temperature threshold to neglect spectra at temperatures warmer than 0°C .

3.1.2 Validating peak finding parameters

To confirm that the peak finding algorithm is working accurately, we examine the number of peaks identified per pixel against a spectrogram. An example of the results from this comparison are shown in Fig. 7. Panel (a) shows the number of peaks detected at each range gate, panel (b) shows the modal number of peaks for that profile and panel (c) shows the identified peaks marked on the main spectrogram by the black points. The grey shading shows where the turbulence threshold has been exceeded (described in Sect. 2.1.2); it is possible to see that these shaded areas correspond to narrow bands of the spectrogram

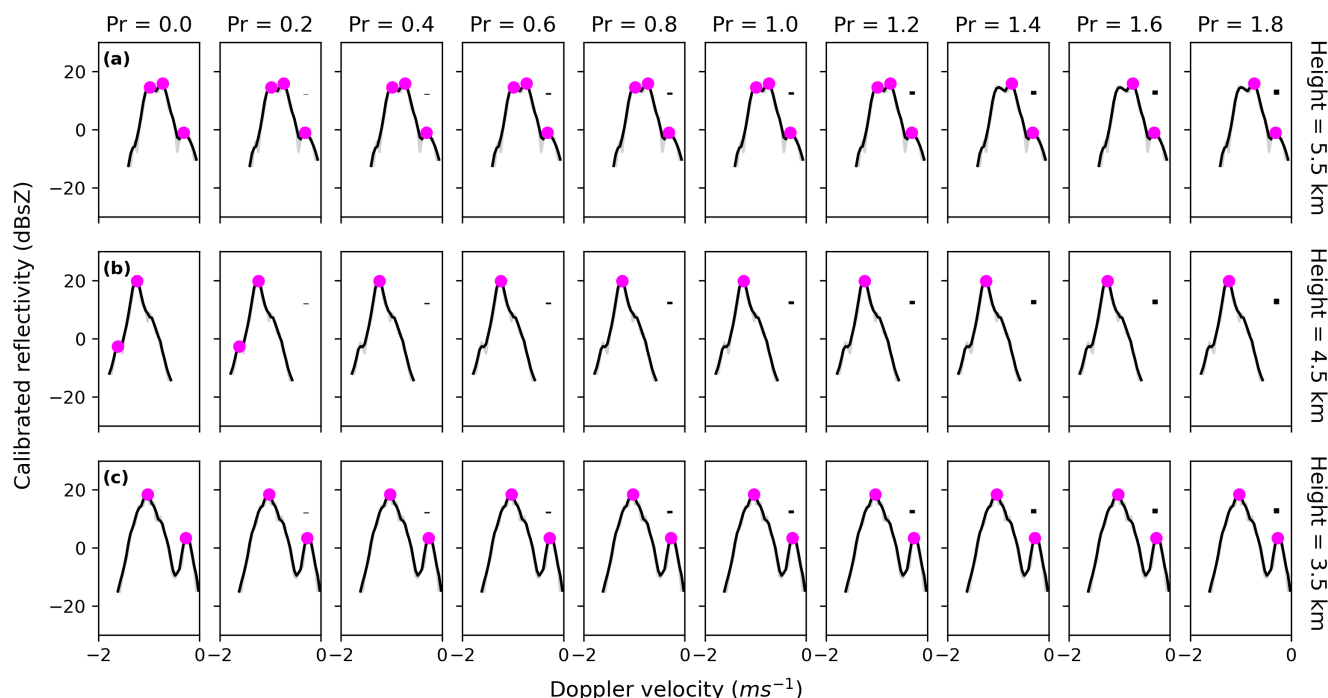


Figure 6. As Fig. 5, but showing the effect of changing the prominence (Pr) parameter. The window length for the moving average is fixed at three velocity bins. The one dimensional Doppler spectra are at heights of 5.5 km (a), 4.5 km (b) and 3.5 km (c) from the example shown in Fig. 1. The prominence value is varied and displayed above each column (see text and Table 2 for description). The thick black line in the top right corner of each panel shows the scale of the prominence thresholds relative to the spectra.

which appear to have been smudged and, in the case of the example at 3.6 km, have lost the distinction between the two particle
 250 populations. We find from panel (a) that generally the algorithm can correctly identify the difference between monomodal and multimodal spectra, but the exact number of peaks detected is a little noisy. We therefore assess for spatial and temporal continuity by calculating the modal number of peaks in a vertical span of 240 m (four range bins) and temporal span of 10 minutes (10 individual spectra). The dimensions for this modal window were varied to test whether the the results change with a change in these dimensions. We found that using a window that included half or double the amount of pixels had very little
 255 impact on the results presented later (not shown for brevity); this gave us confidence that the peak finding results are not highly sensitive to the exact figures chosen here. Panel (b) shows that the modal number of peaks for this spectrogram is significantly more consistent with height compared to the raw results in panel (a). The modal number of peaks indicates multimodality at 3–4 km and 5.5–6 km, which appears well correlated with the areas on the spectra in panel (c) in which multiple particle populations are visible. From 4–5.5 km, the modal number of peaks is consistently representative of a monomodal population,
 260 which is supported by the narrow width of the spectrogram shown in panel (c) in the same region. The location of the peaks on



the main spectrogram in panel (c) provide additional evidence that the algorithm is working accurately because we see that the identified peaks are aligned with the peaks in spectral reflectivity that are determinable by eye.

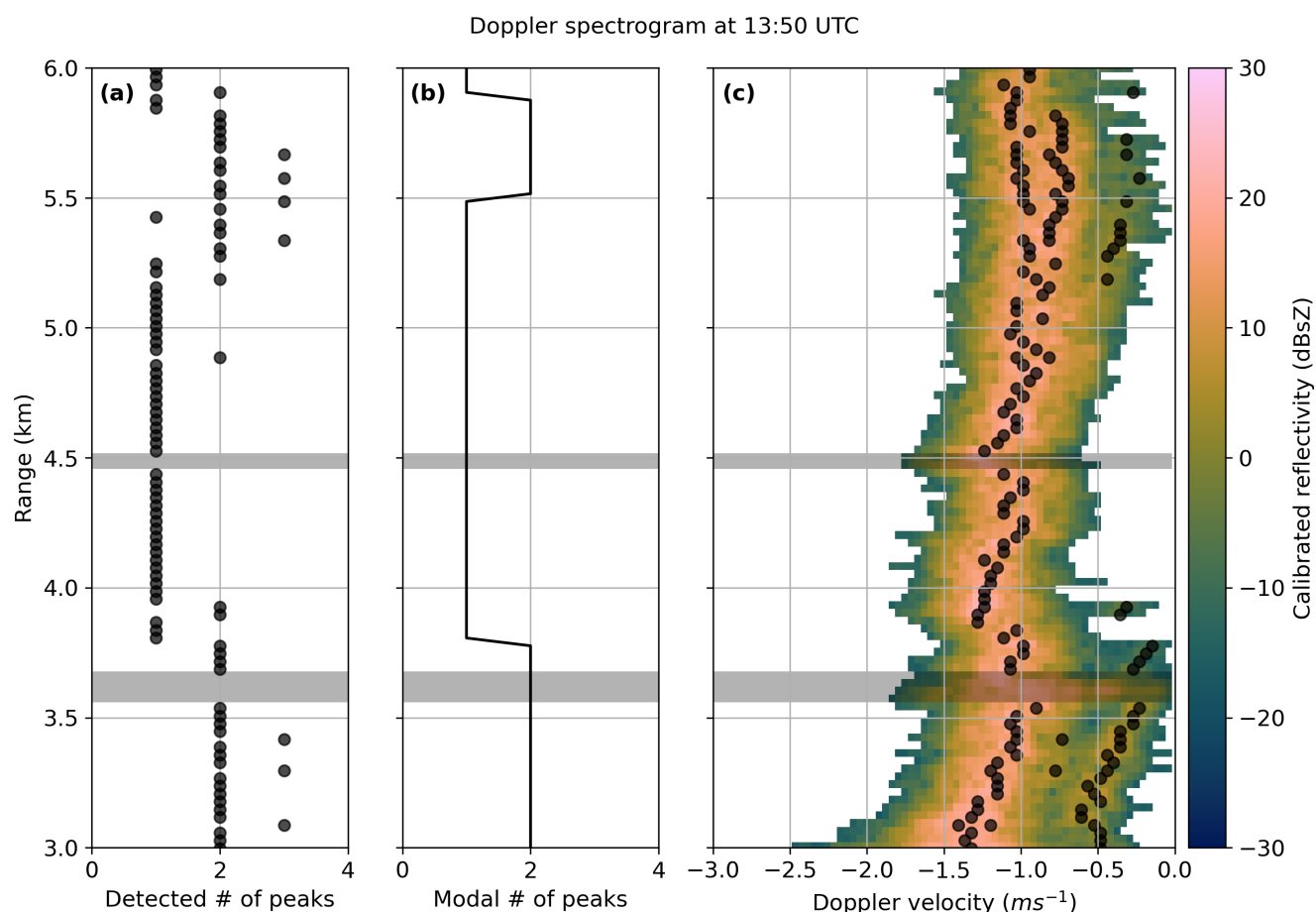


Figure 7. The number of peaks identified in each range gate is shown in panel (a), the modal number of peaks in a 240 m and 10 minute window in panel (b), and the location of identified peaks on the main spectrogram of the example described in Sect. 2.1.1 is shown in panel (c). The grey shading in each threshold shows where the turbulence threshold has been exceeded (see Sect. 2.1.2).

3.1.3 Separating particle modes

The peak finding method not only provides an estimate of the number of peaks identifiable in each spectrum, but also the velocity at which these peaks occur, from which the spectral reflectivity of these peaks is also discernible. This provides a wealth of information about the individual particle populations that would not be available from knowing solely the number of identified peaks per pixel. The primary population is identified based on the assumption that this population has the greatest spectral reflectivity. We therefore assign any population at slower velocities than the primary population to the ‘slow mode’ and

265



any populations at faster velocities to the ‘fast mode’. Whilst this method generally provides an accurate estimate of the primary
270 and secondary velocities, there are times when the diagnosis of primary and secondary peaks can be ambiguous. This happens
when there are two populations with very similar spectral reflectivities, so that the spectral reflectivity of one population is not
consistently bigger than the other. However, the proportion of these ambiguous cases is very small, and therefore has a limited
impact on the analysis that is performed using these results.

4 Results and Discussion

275 In this section, we present two case studies in detail, chosen to represent the variation observed among the selected case
studies outlined in Table 1. We present standard moment level data for each case to help provide context, then show the
results from our peak finding method described in Sect. 3.1. We qualitatively assess the findings from these two examples
and discuss the mechanisms that may be responsible for the multimodal spectra observed in these cases. Using results from
all cases, we then provide a quantitative estimate for the distribution of identified multimodal spectra with temperature. We
280 analyse the peak velocities identified using the peak finding technique to investigate how the vertical velocity of particles
varies between monomodal and multimodal regimes. This is then compared to the vertical distribution of MDV to assess the
influence of multimodal particle populations on measurements of MDV. This has applications for interpretation of data from
ground based instruments, but also for spaceborne Doppler radar such as that on the Earth Cloud, Aerosol and Radiation
Explorer (EarthCARE) satellite (Illingworth et al., 2015; Wehr et al., 2023).

285 4.1 Case study: 6 January 2017

On 6 January 2017, an area of relatively deep low pressure, centred between Iceland and Scandinavia, was associated with a
complex multi-fronted system. A warm front and two occluded fronts associated with this system passed over the UK before
meeting a blocking high pressure centred over Central Europe. An ice cloud associated with these fronts was observed, which
was up to 7 km deep above the melting layer (which remained at around 2 km throughout the day). Moment level observations
290 of this cloud made by the Copernicus radar (described in Sect. 2.1) are shown in Fig. 8. Here we show the reflectivity in Fig. 8a,
MDV in Fig. 8b, and spectral width in Fig. 8c. We see that a thin layer of low level cloud is present for several hours during the
first half of the day along with some upper level cirrus, before the thick frontal cloud comes into the view of the radar at around
13:00 UTC and persists for the rest of the day. There are hints of microphysically interesting features in this cloud such as
discernible regions of increased spectral width that correspond to ‘streaks’ in the reflectivity and changes in MDV, for example
295 between 14:00 and 17:00 UTC and between 21:30 and 23:30 UTC at heights of approximately 2–3 km. There was moderate
rainfall associated with this cloud, shown in Fig. 8d, which started at 14:00 UTC and continued for the rest of the day, reaching
peak values of $\sim 4 \text{ mm hr}^{-1}$ between 23:00 and 00:00 UTC.

Microphysical features, such as those mentioned above, can be investigated in greater detail using the results from the peak
finding method described in Sect. 3.1. From this method we have an estimate of the number of peaks observed in the Doppler
300 spectra for each pixel in a cloud, and the Doppler velocities for both the primary and secondary populations. The results from

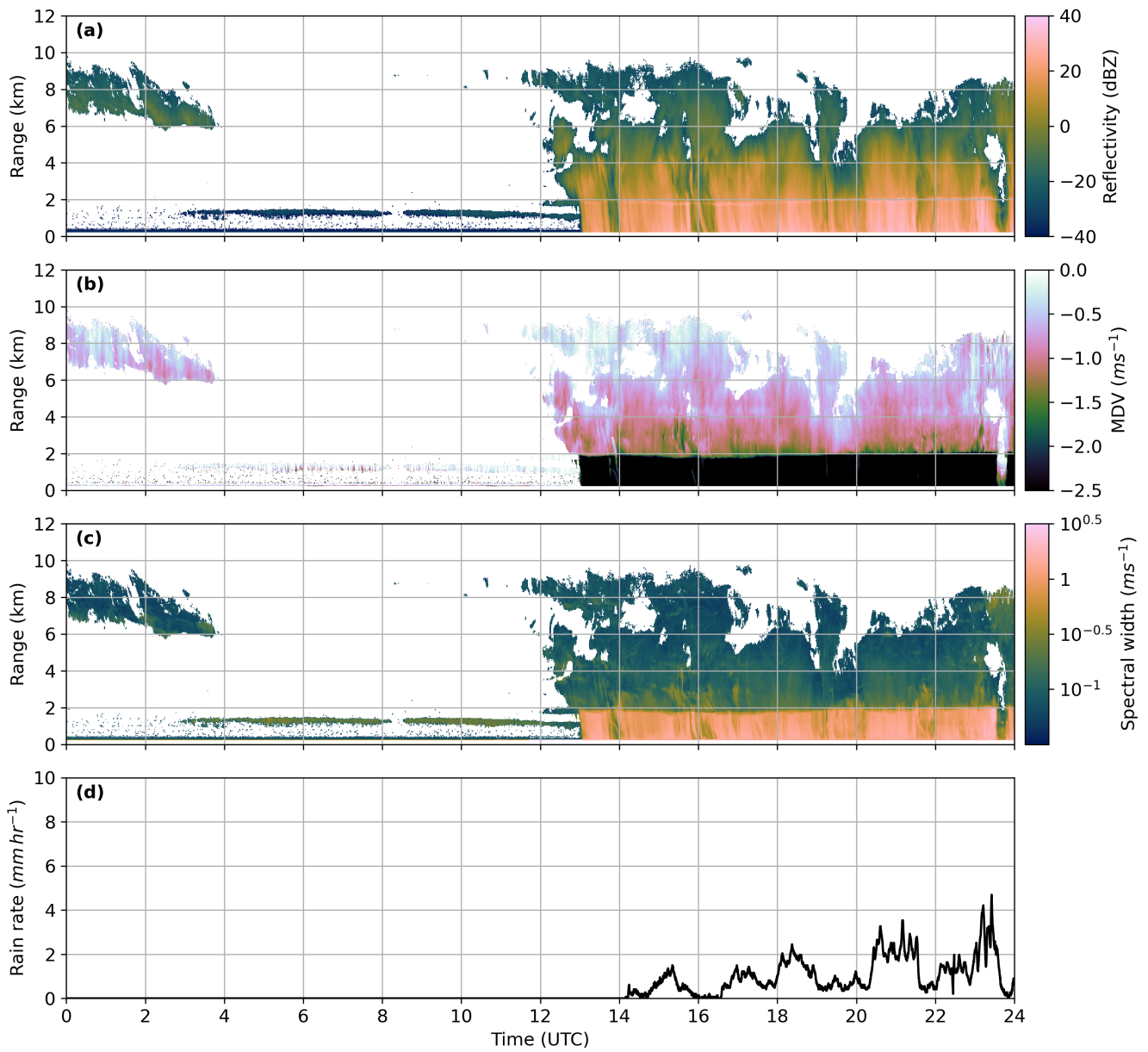


Figure 8. Moment level observations of reflectivity (a), mean Doppler velocity (b) and spectral width (c) from the Copernicus radar and rain rate (d) measured at CFARR for 6 January 2017.



this analysis are shown in Fig. 9. Figure 9a shows the number of identified peaks per pixel, Fig. 9b shows the velocity of the primary population and Fig. 9c shows the velocity of the slower falling mode of particles. When a trimodal spectrum with two slower falling particle modes is identified, the faster of these slow modes is shown in Fig. 9c as we assume this mode is associated with ice particles instead of a drizzle mode, which would likely have very low fall speeds (Zawadzki et al., 2001).

305 Temperature contours from archived ICON data are shown in blue on all panels. We find that multimodal spectra are frequent between the temperatures of -5°C and 0°C from around 14:00 UTC until the end of the observed period. It is interesting that the number of peaks also increases with increasing temperature in some parts of this layer; there is a visible shift from bimodal to trimodal spectra with increasing temperature at 14:00–15:00 UTC, 17:30–18:30 UTC and 19:00–20:00 UTC. Inspection of spectrograms at different times, for example that shown in Fig. 10, reveal that there were indeed a mixture a bimodal (Fig. 10a) and trimodal (Fig. 10b) spectra observed on this day. At temperatures between -5°C and -15°C , there are a handful of isolated regions with multimodal spectra at approximately 14:00–15:00 UTC and 20:00–21:00 UTC. Multimodal spectra are almost non-existent at temperatures colder than -15°C . An understanding of the microphysical processes that are active in this case may be gained by examining the velocities in Fig. 9b–c. We find at temperatures lower than -5°C , primary velocities remain consistent with height. At temperatures greater than -5°C , we see that velocity increases as the particles fall with velocities

315 reaching -1.5 to -2 m s^{-1} . These increases in velocity are correlated with the presence of multimodal spectra. This suggests that the process responsible for producing multimodality in the Doppler spectra is connected to the increased primary mode fall speeds. Riming causes increased particle fall speeds due to increased mass, without causing particles to grow much in size; this is because it acts to ‘fill in the gaps’ of open structured particles such as dendrites and aggregates before adding to the overall size (e.g. Garrett and Yuter, 2014; Kneifel and Moisseev, 2020). Riming necessarily occurs in environments which are

320 saturated with respect to liquid water, and therefore splinters produced by rime splintering rapidly undergo vapour growth to form needle and column crystals which fall at a distinctly slower speed than the rimed population. If they grow large or fast enough, the needle and column crystals themselves will begin to rime.

Example spectrograms shown in Fig. 10 support these suggestions. Figure 10a shows clear evidence that a secondary particle mode is visible at heights of approximately 2–2.5 km, which corresponds to temperatures of approximately -3°C to 0°C . This

325 secondary mode consists of ice particles as it melts at 0°C , as evidenced by the rapid increase in fall velocity of the population. The primary population has a relatively high and consistent fall velocity of approximately -1.5 m s^{-1} between temperatures of -10°C and 0°C , suggesting riming is influencing the fall velocity of this population. Figure 10b shows evidence that both a secondary ice mode and a drizzle mode are present at this time, which corresponds to a region where trimodal spectra were identified (shown in Fig 9a). The drizzle mode is first visible at 2.5 km, and is identifiable as the fall velocity of the population

330 does not rapidly increase at the melting layer, and indeed remains separate in the rain below. This therefore agrees with the suggestion that rime splintering is responsible for the multimodal spectra observed in this here; cloud droplets are required to form and grow drizzle drops, so the presence of drizzle shows clear evidence that there is liquid water present at temperatures associated with rime splintering and that liquid water droplets are therefore available for riming.

Calculating an average daily spectrogram can provide further evidence for persistent microphysical features that may be

335 visible in the individual spectra; Fig. 10c shows the average spectrogram for this case study, with the average MDV shown by

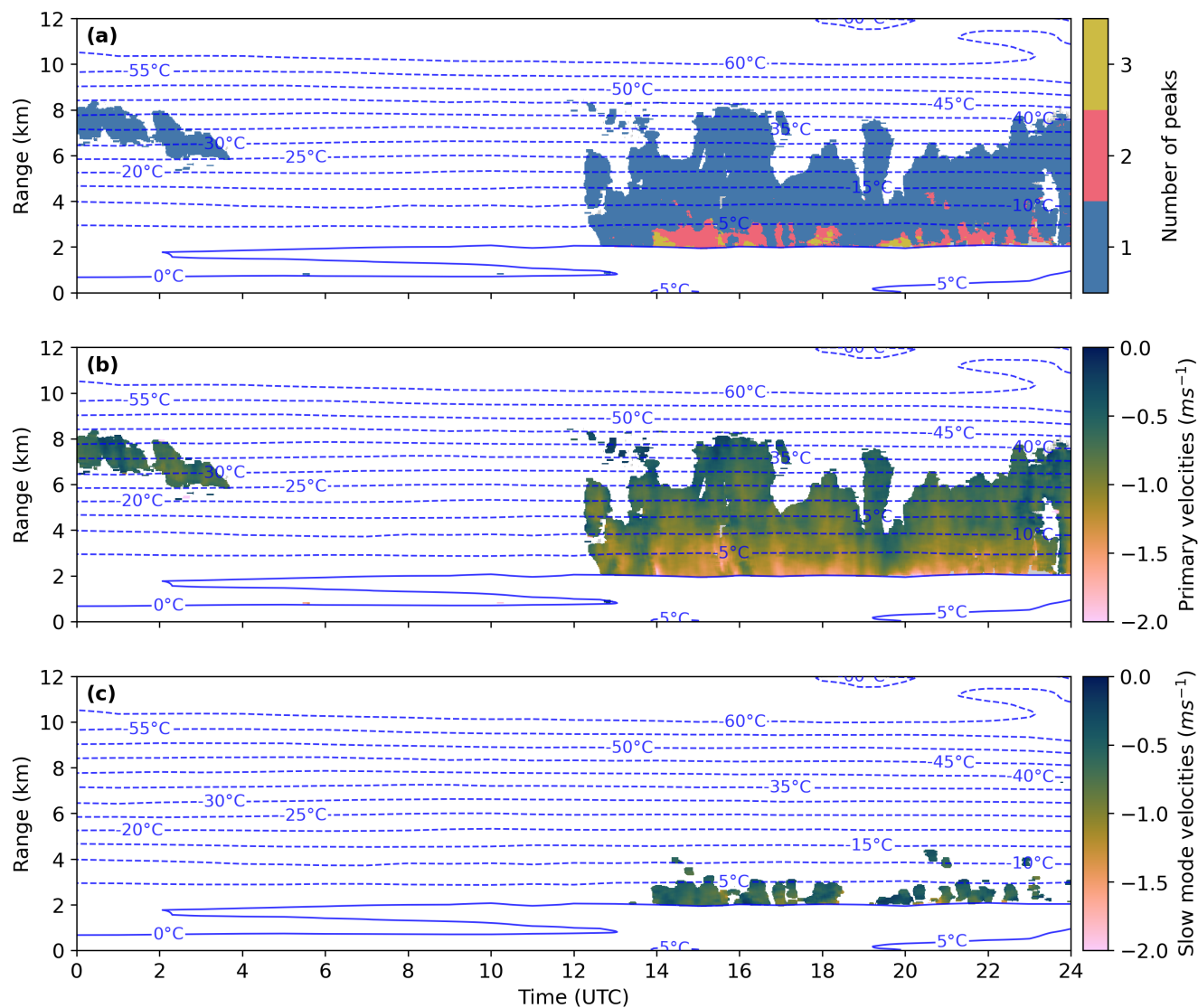


Figure 9. Number of peaks identified by the peaks finding method (a), velocity of the primary population (b) and velocity of the slower-falling particle mode (c) for 6 January 2017. The grey shading in (a) and (b) shows cloud pixels that were removed during filtering for turbulence and attenuation; this is only visible in very small patches in this cloud (for example 23:00 UTC at 2 km) but is clearer in later examples.

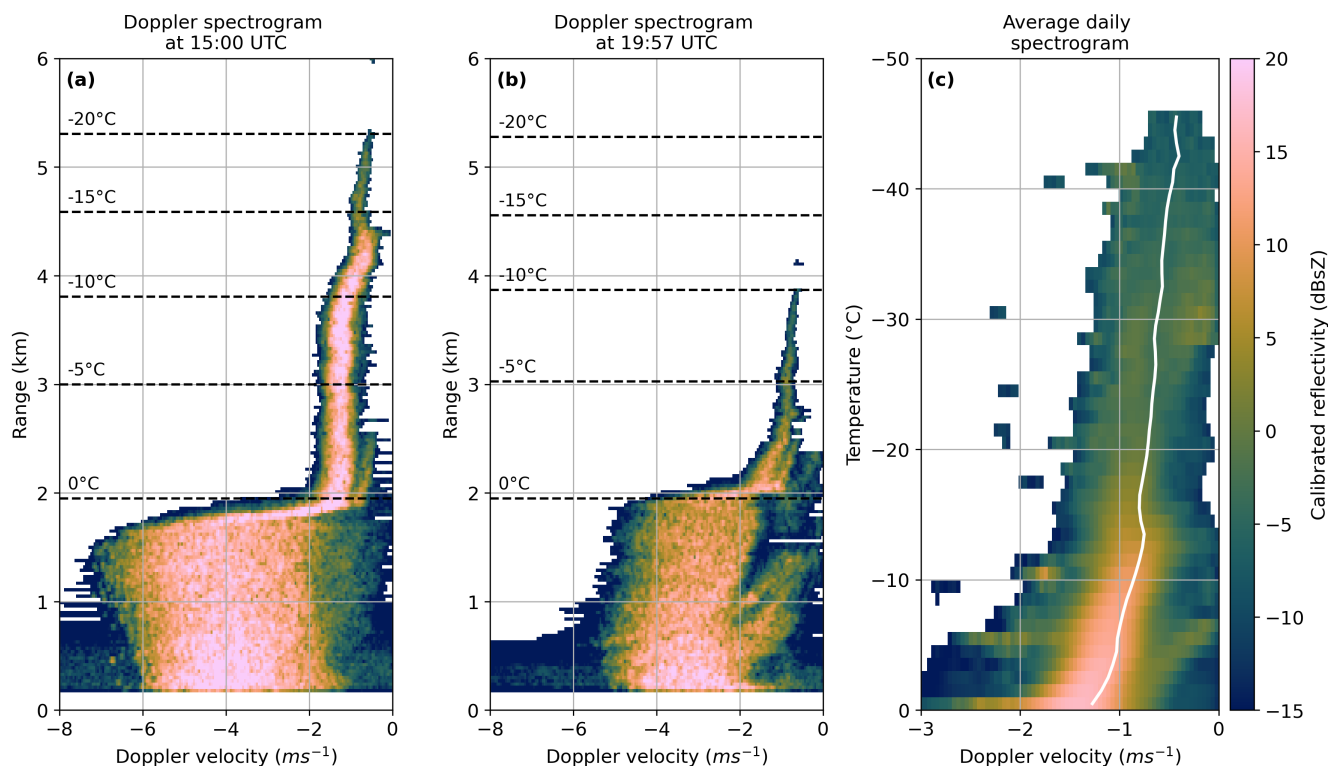


Figure 10. Examples of spectrograms with bimodal (a) and trimodal (b) signatures, and an average spectrogram (c) for 6 January 2017. In (c), the average MDV is shown by the white line and the vertical axis has been converted to temperature so that temperature dependent microphysical features are not smoothed out as temperature surfaces vary in height. Turbulent and high attenuation regions have been removed.

the white line. We find that particle velocities gradually increase from the top of the profile to around -17°C , where a slight decrease in velocity is apparent and reaches a minimum at approximately -13°C . The potential mechanisms responsible for this feature are discussed in greater detail in Sect. 4.4. Particle velocities increase again from around -13°C to 0°C . Very clearly visible is the secondary population that forms at approximately -7°C and increases in speed as temperature increases, but never quite reaches the same speed as the primary population. This agrees with the results shown in Fig. 9a, where persistent multimodality is observed between -5°C and 0°C . The presence of this secondary population and the increase in particle velocities seen throughout this layer reinforces the suggestion that riming is the dominant source of secondary particles at these temperatures via the rime splintering mechanism.

4.2 Case study: 17 May 2017

On 17 May 2017, low pressure conditions were dominant over the UK resulting in several frontal features which passed over the UK throughout the course of the day. Associated with these frontal features was a long-lived ice cloud which was up to



8 km deep above the melting layer and which persisted for the majority of the day. The melting layer was at about 3 km and dropped slightly in height throughout the day. Moment level observations of this cloud are shown in Fig. 11, with reflectivity in Fig. 11a, MDV in Fig. 11b and spectral width in Fig. 11c. At a glance, this appears to be a more homogenous cloud than
350 that in the previous case study, with fewer clear microphysical features. There is a region at 5–6 km between 10:00 and 15:00 UTC with MDV that is lower than the surrounding regions, and the values of MDV observed here are less than -0.5 m s^{-1} . Interestingly, Fig. 12b shows evidence that the velocities of the primary population also decrease in the same region. We see that there are increased values of spectral width at 13:00 UTC which correspond to a disturbance of the melting layer which is visible in Figs. 11a–b. Figure 11d shows the rain rate, which remains moderate to heavy throughout the day, with an intense
355 shower at 13:00 UTC. This very heavy shower corresponds with the disturbance in the melting layer visible in Figs. 11a–c, which suggests that this feature is a cell of embedded convection. Figure 2 shows that the turbulent contribution to spectral width is high in this region, and is therefore removed when the turbulent filtering method described in Sect. 2.1.2 is applied.

The results from the peak finding method can again be used to infer what processes are influencing the development of this cloud, and are presented in Fig. 12. Figure 12a shows the number of identified peaks, Fig. 12b shows the velocity of the
360 primary population and Fig. 12c shows the velocity of the slow mode. We see that the distribution of multimodal spectra in this example is different to the that examined in Sect. 4.1. Almost all multimodal spectra are bimodal, except a few isolated regions early in the observation period which are trimodal. From Fig. 12a, we can see that at temperatures between -5 and 0°C , multimodal spectra are prevalent throughout much of the cloud. Similarly to the case analysed in Sect. 4.1, there is evidence to suggest that this multimodality is associated with riming, as there are increased primary velocities visible in Fig. 12b that are
365 consistent with particles influenced by riming; particle velocities are approximately -1.5 m s throughout much of the cloud layer at temperatures between -5 and 0°C . The slow mode velocities in this layer, shown in Fig. 12c, appear to increase slightly with temperature. The presence of the slow particle mode and its increase in velocity with temperature strengthens the argument that riming is active at these temperatures, so it is reasonable to suggest that rime splintering may also be active and controlling the presence of the slow particle mode. We also find that between temperatures of -10 and -15°C there are frequent multimodal
370 regions. The mechanism behind this multimodality is unclear, as this is outside the temperature range which is expected for the rime splintering mechanism. The velocity of the secondary population at these temperatures is very slow at around -0.25 m s^{-1} . As dendritic growth is preferential at these temperatures, it follows that the slow particle mode may consist of small plate-like or dendritic particles which fall slowly due to relatively large surface areas resulting in increased air resistance.

Figure 10 shows two examples of spectrograms observed during this case study. In Fig. 13a, a secondary population is visible
375 that forms at approximately -7°C and increases in fall velocity, but remains distinct from the primary population. In Fig. 13b, it is possible to see a secondary population which forms at -15°C and grows until the velocity becomes indistinguishable from the primary population at approximately -10°C . Another secondary population is visible from around -7°C to the melting layer. It is clear that the secondary populations shown in Fig. 13a and Fig. 13b are ice as they rapidly increase in the melting layer, thus suggesting that drizzle is not prevalent in this case; the lack of trimodal spectra seen in Fig. 12a supports this idea.

380 The average spectrogram for this case shown in Fig. 13c shows an increase in particle velocities through the upper regions of the cloud, from around -0.4 m s^{-1} at -50°C to -1 m s^{-1} at -16°C . Like in Fig. 10, we see a slight decrease in the average

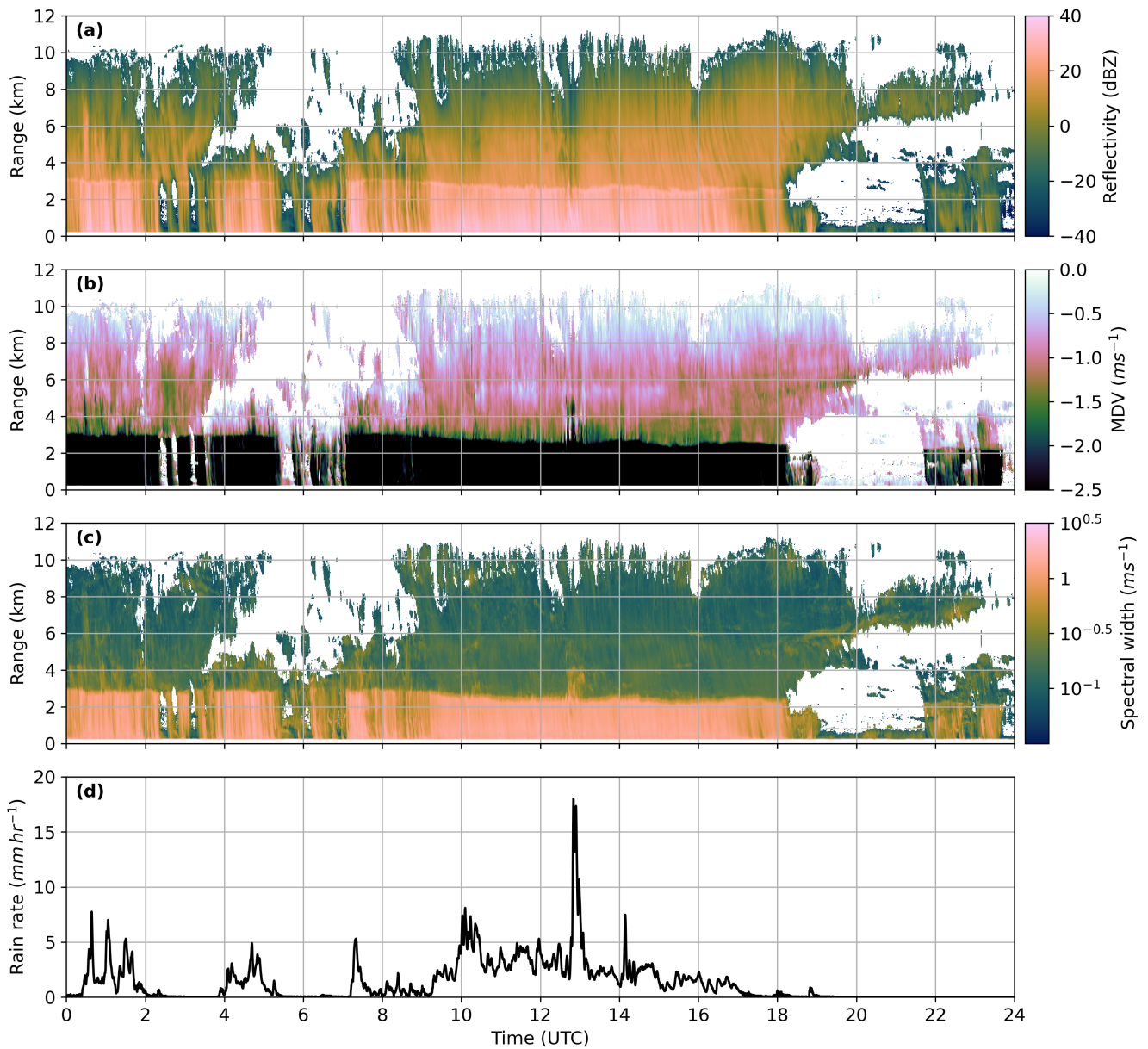


Figure 11. As Fig. 8, for 17 May 2017.

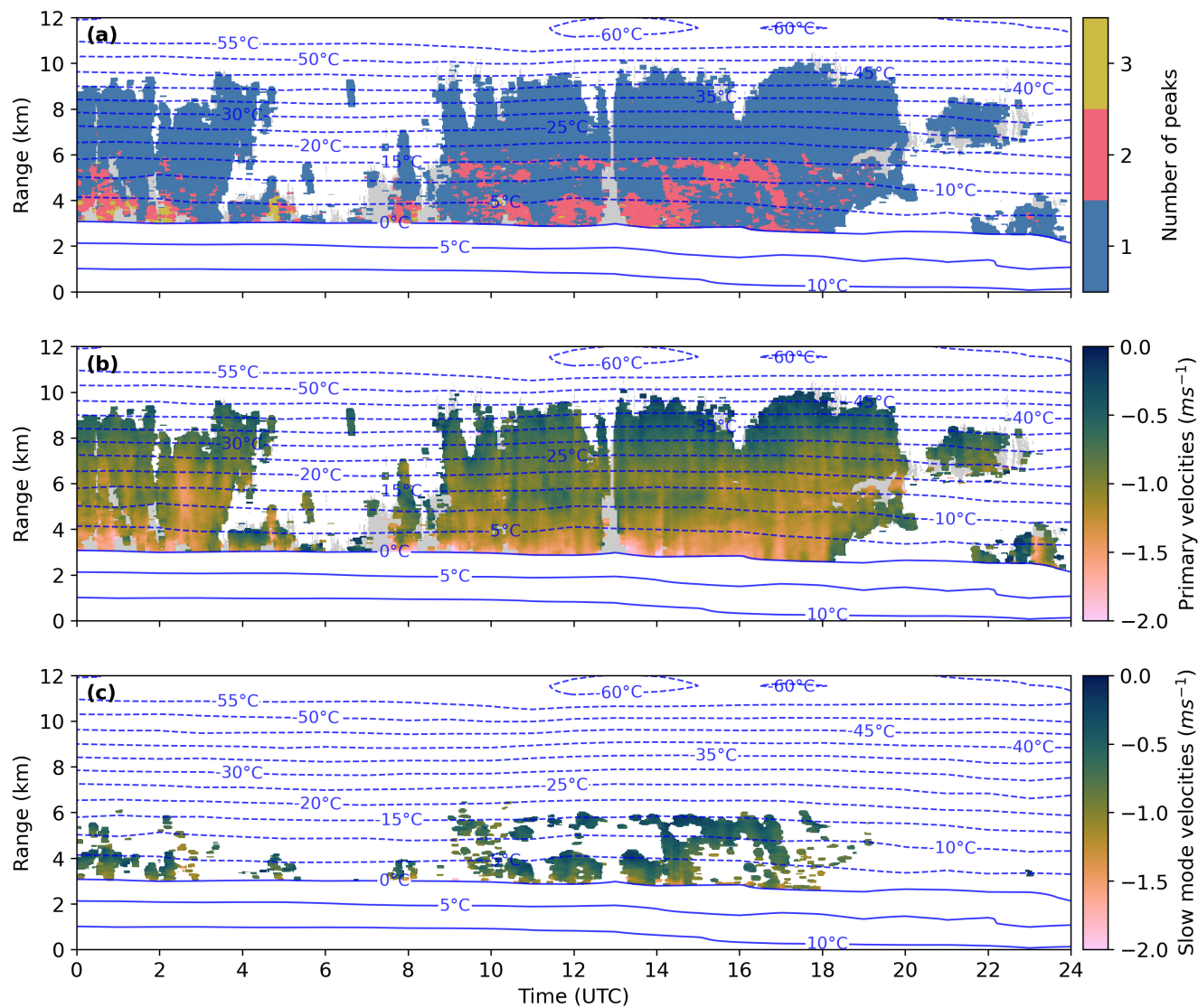


Figure 12. As Fig. 9, for 17 May 2017.

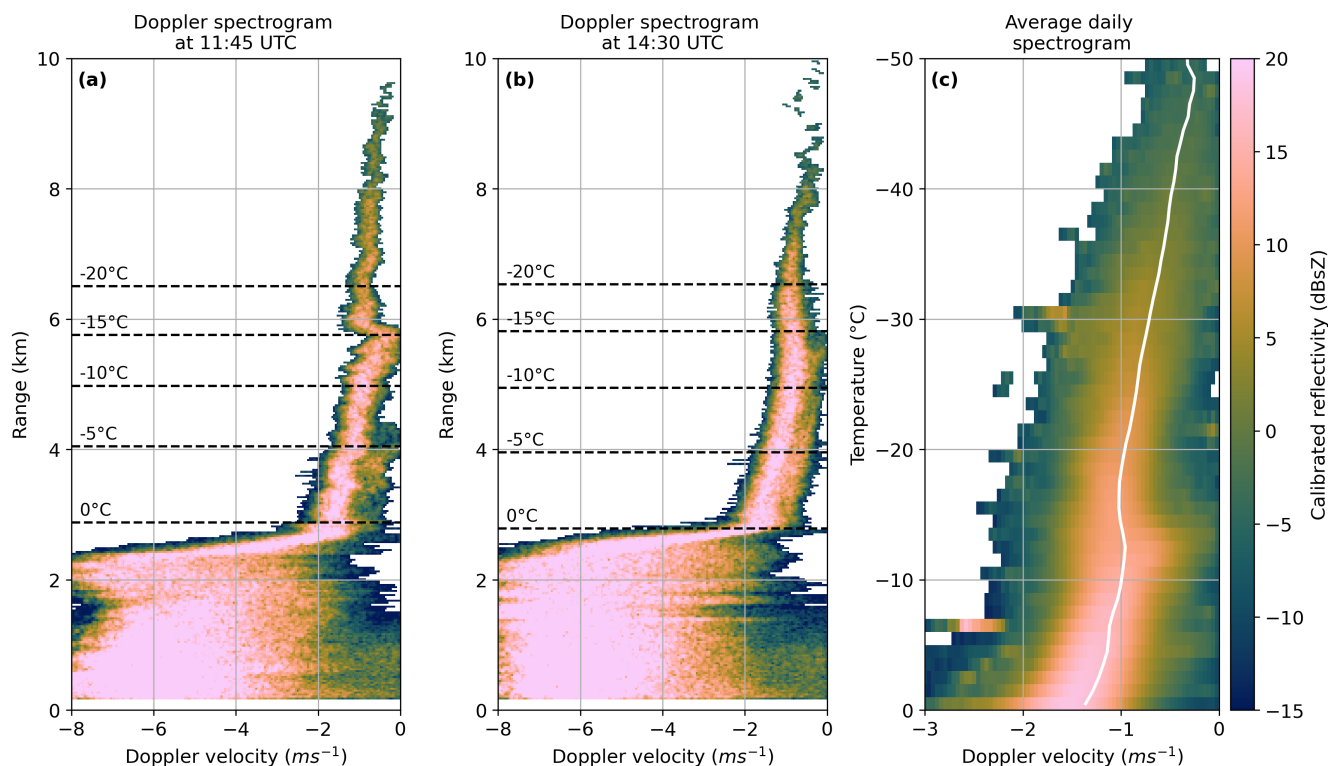


Figure 13. Examples of spectrograms with bimodal signatures at -5°C (a), both -5°C and -15°C (b), and an average spectrogram (c) for 17 May 2017. In (c), the average MDV is shown by the white line and the vertical axis has been converted to temperature so that temperature dependent microphysical features aren't smoothed out as temperature surfaces vary in height. Turbulent and high attenuation regions have been removed.

MDV from -16°C to -13°C ; whereas this feature is evident in Fig. 13a by the decreased velocities at -15°C , the effect is less pronounced when averaged over a whole day. Also visible in this region is evidence for the formation of a secondary population, as there an increase in the width of the spectrogram with high spectral reflectivity. This agrees with the location
 385 of the peaks detected by the peak finding algorithm shown in Fig. 12a. Interestingly, the secondary populations detected at warmer temperatures (-5 to 0°C) are not clear in this averaged spectrogram. This is likely because the secondary population at these temperatures is only present for part of the day and the signal is therefore weakened by the averaging process, but there is a weak signal visible at slow velocities between temperatures of approximately -8°C and 0°C .

4.3 Statistics from all case studies

390 In Sects. 4.1 and 4.2, we have qualitatively analysed the distribution of multimodal spectra with temperature, and discussed possible mechanisms influencing the development of the clouds in these case studies. In order to make these findings applicable more generally, it is useful to quantify the distribution of multimodal spectra with temperature across all of the case studies



outlined in Table 1. We therefore calculate an estimate of the fraction of ‘in-cloud’ pixels where multimodal spectra are observed and the results of this analysis are shown in Fig. 14. The grey lines show the results for individual case studies, and the black line shows the overall statistics. To the best of our knowledge, the frequency of observed multimodal spectra has not been quantified in this way previously.

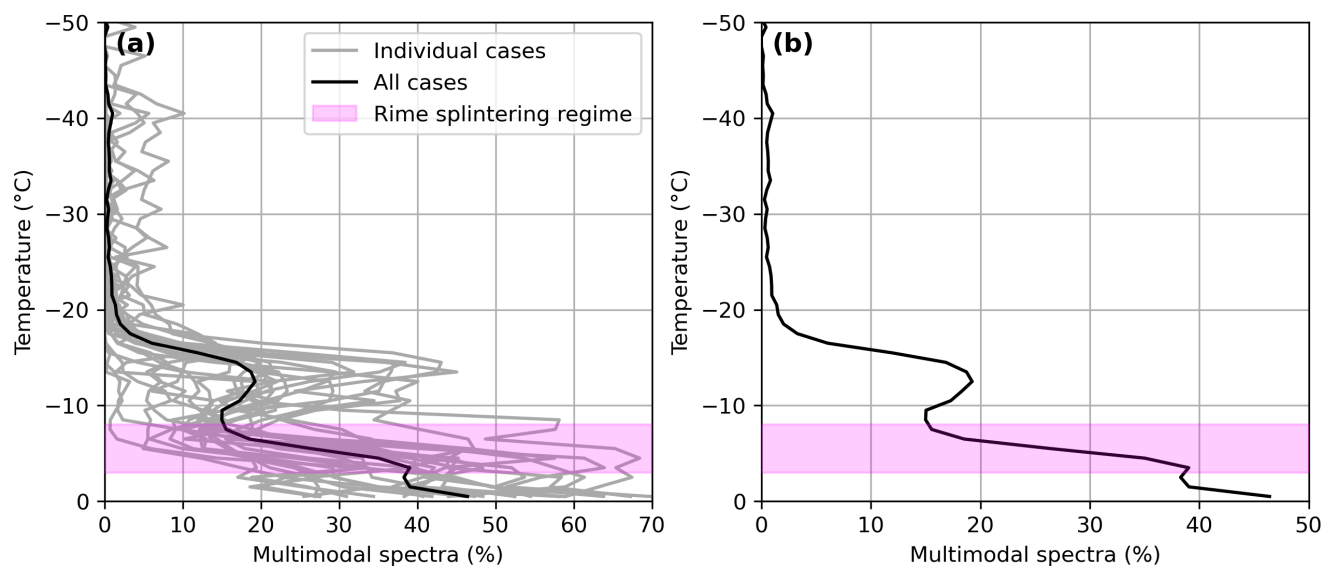


Figure 14. Percentage of ‘in-cloud’ pixels with observed multimodal spectra. (a) The grey lines show the results for individual cases, and the black line shows the statistics across all case studies. (b) The distribution from all case studies is shown individually for clarity. The rime splintering regime is shown in magenta (based purely on temperature). Note the different x-axis limits between panels.

The magenta shading in this figure highlights temperatures from -3°C to -8°C , which is the temperature range in which it is thought that the rime splintering mechanism is active (Field et al., 2017; Korolev and Leisner, 2020, and references therein), and indeed previous studies have shown evidence from in situ observations of particles consistent with rime splintering being observed at these temperatures (e.g. Crosier et al., 2011, 2014; Keppas et al., 2017; Mammatt et al., 2026). We see that throughout this temperature regime, the percentage of multimodal spectra increases rapidly from approximately 15 % at -8°C to 40 % at -3°C . The percentage of multimodal spectra continues to increase at temperatures higher than this ice multiplication regime, which suggests that secondary particle populations continue to grow and evolve throughout this relatively narrow temperature band before reaching the melting layer. Individual cases vary in the magnitude of the percentage of multimodal spectra throughout this regime, but all follow broadly the same pattern.

At temperatures of -10°C to -18°C , we see an increase in the percentage of multimodal spectra from less than 5 % at -18°C to a maximum of 20 % at -13°C . This is outside of the temperature range that the rime splintering mechanism is thought to be active in, so we expect that a different mechanism is causing the observed multimodality. It is possible that new particles at these temperatures are formed by primary nucleation, but this raises the question of why primary nucleation



410 would consistently occur in this region. There is a lack of evidence in the current literature that ice nucleating particle (INP) concentrations increase at these temperatures, and instead observations have shown evidence that INP concentrations decrease with decreasing temperature (e.g. DeMott et al., 2010). There have been studies which show that conditions here are potentially favourable for SIP; droplet fragmentation and ice-ice collisional fragmentation have been suggested as potential mechanisms for the production of secondary ice particles at temperatures outside the rime splintering regime (Field et al., 2017; Korolev and 415 Leisner, 2020). Droplet fragmentation has received some attention in recent years (Phillips et al., 2018; Keinert et al., 2020; Lauber et al., 2021), and occurs when a drizzle drop spontaneously freezes and projects splinters as a result of a shattering ice shell. This process is unlikely to be the primary cause of multimodality observed at these temperatures, as we have seen very little evidence for a drizzle mode visible in the Doppler spectra at these temperatures. Trimodal spectra, which are likely to indicate the presence of a drizzle mode (see Fig. 10a), are only detected at temperatures warmer than -5°C in Fig. 9a and there 420 is very little evidence for drizzle in Fig. 12a. Ice-ice collisional breakup has also been proposed as an efficient SIP mechanism (Vardiman, 1978; Yano and Phillips, 2011; Yano et al., 2016; Phillips et al., 2017), in which ice fragments are produced during collisions between ice particles. Dendritic growth on particles precipitating from above produces fragile branches which may be susceptible to fragmentation, and the fragments produced may have the potential to grow into a secondary particle mode. Whilst there have been laboratory studies carried out previously to investigate these processes, a lack of observational in situ 425 evidence means uncertainty surrounding the efficiency and feasibility of these mechanisms remains high.

Multimodal spectra are very rare at temperatures lower than -20°C , which is in agreement with previous studies which have shown evidence to suggest that SIP is very inefficient at low temperatures (Field et al., 2017; Korolev and Leisner, 2020). However, Korolev et al. (2022) presented a case study of a precipitating cirrocumulus-nimbostratus cloud system with generating cells of turbulence, and suggested that SIP can be observed at temperatures as low as -27°C . This demonstrates the 430 continued importance of investigation into SIP processes active outside of the rime splintering regime.

4.4 Vertical profiles of peak velocities and MDV

The velocities associated with the peaks identified by the peak finding algorithm can help us gain understanding into how these vary with height; these velocities will be referred to as peak velocities throughout this section, as they are the velocity at which the peak spectral reflectivity is observed. It is possible to separate the peak velocities into the different populations they 435 represent, as described in Sect. 3.1.3, and in Fig. 15 we therefore show histograms of all peak velocities (a), all primary peak velocities (b), primary peak velocities from monomodal spectra (c), primary peak velocities from multimodal spectra (d) and slow mode velocities (e) against temperature. The medians from Figs. 15a–e are shown in Fig. 15f to facilitate simple comparison. This analysis shows some interesting features. We see from Figs. 15a–c that the vertical profile of all peak velocities, all primary peak velocities and monomodal primary velocities is generally similar, and Fig. 15f shows that the medians are 440 frequently indistinguishable from each other. This suggests that the influence of secondary peaks on the overall distribution of velocities (Fig. 15a) is modest, but there are differences which demonstrate that this cannot be neglected. Here, we see that velocities in Fig. 15a–c increase with temperature from -50°C , where the median velocity is approximately -0.6 m s^{-1} , to -18°C , where the median velocity is around -0.9 m s^{-1} . There is a clear decrease in velocity between -18°C and -13°C , where



the median velocity falls to around -0.8 m s^{-1} . Whilst this appears to be a small change, this equates to an 11 % reduction
445 between the velocity at -18°C and at -13°C . We attribute this feature to dendritic growth on particles precipitating from above
– that is, the growth of dendritic branches on polycrystals and aggregates formed at lower temperatures. These geometrically
open dendritic features experience greater drag force than other crystal growth habits, and therefore fall more slowly for a pro-
jected area to given mass ratio (Heymsfield and Westbrook, 2010). From this velocity minimum at -13°C , the median velocity
increases with temperature for the rest of the profile, however the temperature range between -10°C and 0°C is where we
450 see the greatest differences between these profiles. Figure 15a shows that the median velocity remains approximately constant
at -1.1 m s^{-1} between -8°C and -3°C , before increasing to -1.5 m s^{-1} at 0°C . In contrast, the median velocity in Fig. 15b
increases mostly consistently from -1.0 m s^{-1} at -10°C to -1.3 m s^{-1} at 0°C . In Fig. 15c, we find that the median velocity
increases gradually from -1.0 m s^{-1} at -10°C to -1.2 m s^{-1} at 0°C .

Figs. 15d–e show velocities associated with multimodal spectra. It is clear from Fig. 15f that the primary velocity from
455 multimodal spectra is consistently higher than from monomodal spectra, remaining higher than -1 m s^{-1} between temperatures
of -20°C and -10°C , and increasing to approximately -1.3 m s^{-1} throughout the rime splintering regime. This may suggest
that riming is influencing the velocity of particles in this temperature regime, although the median velocity remains lower than $-$
 1.5 m s^{-1} ; this is the threshold at which Kneifel and Moisseev (2020) suggest high vertical velocities can be reliably assigned to
riming. Figure 15e shows the velocities of the slow particle mode, and demonstrates clearly the temperatures at which the slow
460 mode is first detectable. The median velocity clearly shows the formation and growth of an appreciable slow falling population
from -15°C , where the median velocity is -0.5 m s^{-1} , to -10°C , where the median velocity has increased to -0.7 m s^{-1} .
Another growth regime is then visible from -5°C , where the median velocity is -0.6 m s^{-1} , to 0°C , where the velocity has
increased to -0.8 m s^{-1} . This provides clear evidence for the existence of multiple populations at these temperatures, with the
slow particle mode increasing in velocity as temperature increases suggesting growing particle size.

465 It is also possible to calculate the distribution with temperature of MDV; Fig. 16 shows this distribution for all spectra
(a), monomodal spectra (b) and multimodal spectra (c). We see from Fig. 16a–b that the profile of MDV with temperature
is very similar in shape, but the median MDV from monomodal spectra is consistently slightly slower than from all spectra
at temperatures higher than -15°C . This is particularly visible in the lowest section of the profile between -5°C and 0°C .
Comparison with Fig. 15a and Fig. 15c shows that these profiles are consistent with the profiles of primary velocities from all
470 spectra and monomodal spectra respectively. Interestingly, we see in Fig. 16c that the median MDV from multimodal spectra
is consistently faster than from monomodal spectra throughout the whole profile, which is in agreement with the increased
primary population velocities seen in Fig. 15d. This provides further evidence to suggest that the mechanism responsible for
producing multimodal spectra acts to increase the velocity of the primary population, and that this has a greater influence
on the MDV in both of the identified temperature regimes than the presence of the slow particle mode. However, monomodal
475 spectra have a greater influence on the overall MDV at this temperature, as evidenced by the decreased MDV at -13°C visible
in Fig. 16a. Figure 14 shows that around 20 % of spectra are multimodal at this temperature, and therefore the majority of
spectra are monomodal.

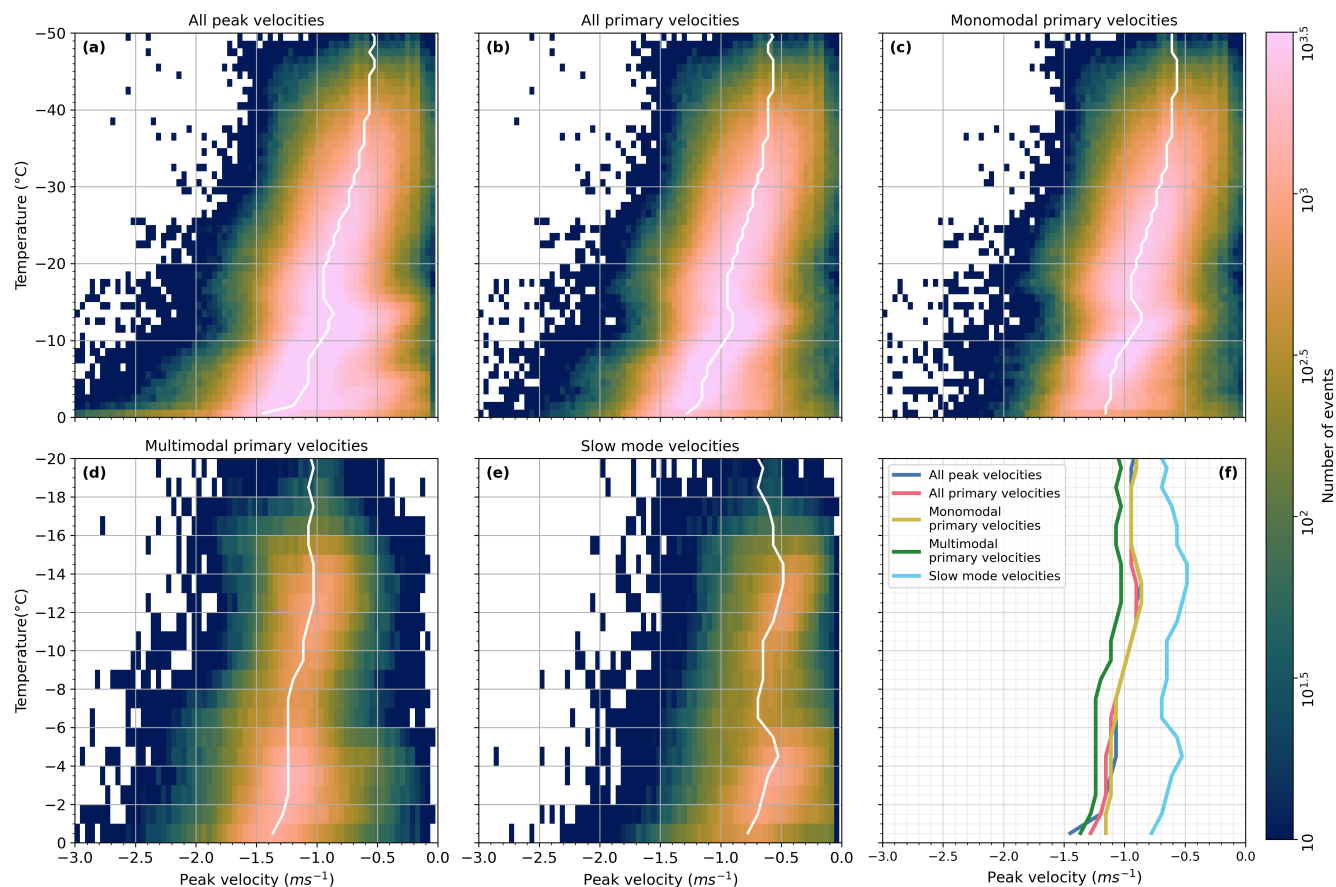


Figure 15. Vertical profiles of particle population velocities as 2D histograms. The white solid line shows the median in panels (a)–(e). Shown are all peak velocities (a), all primary peak velocities (b), primary peak velocities from monomodal spectra (c), primary peak velocities from multimodal spectra (d) and slow mode velocities (e). The medians of all distributions are shown in (f). Note the logarithmic colour scale and change in y-axis limits between the top and bottom row.

Previous remote sensing studies have aimed to characterise the vertical profile of MDV, and have suggested that on average it increases monotonically with increasing temperature. For example, Billault-Roux et al. (2023) calculate vertical profiles of MDV from Doppler radar for separate coexisting particle populations, and provide evidence that this variable generally follows a monotonically increasing profile for the primary particle mode, with small variations at temperatures close to 0 °C. The vertical MDV profile of the secondary modes show greater variation between cases, both in magnitude and profile shape. However, these results were shown for relatively short time periods (in the order of 20 to 30 minutes), where short lived but high-frequency random air motions such as turbulence or gravity waves may influence results (Protat and Williams, 2011). Another example is the statistics of MDV from Doppler radar data presented by Wiener et al. (2024). The data were collected over a 7-year period in Antarctica and the statistics provide evidence that the observed MDV in these cases follows a

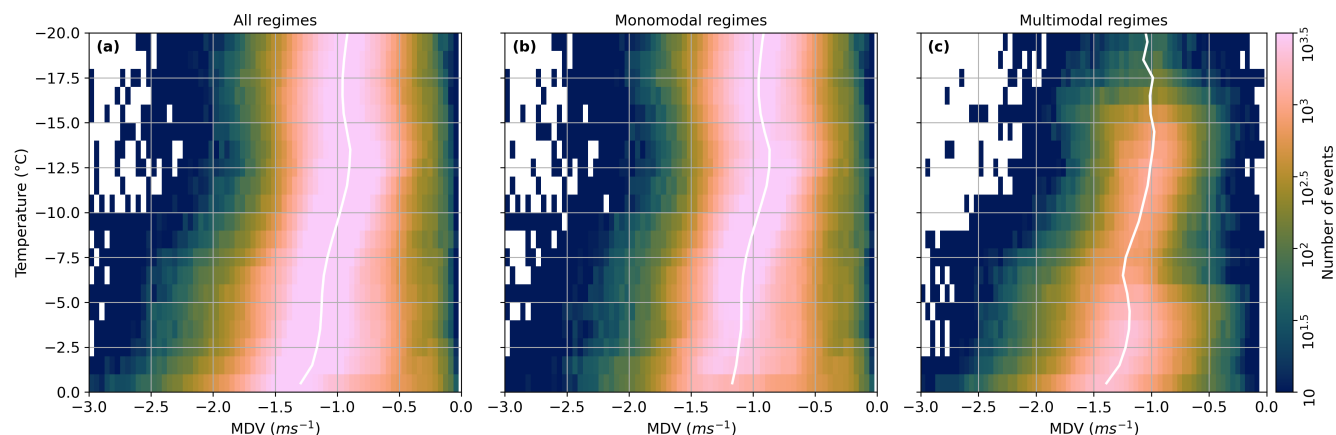


Figure 16. Vertical profiles of MDV as 2D histograms from all spectra (a), monomodal spectra (b) and multimodal spectra (c). The medians of each distribution are shown by the white line. Note the logarithmic colour scale.

monotonically increasing profile. However, the profile of MDV is calculated against height, meaning smaller scale features in the this profile may be smoothed by varying vertical temperature profiles in different atmospheric conditions. Westbrook and Illingworth (2009) provide evidence from a continuous sample of stratiform ice clouds over 17 months that the vertical velocities of ice crystals relative to a $1.5 \mu\text{m}$ Doppler lidar have a strong temperature dependence; particles fall faster at higher temperatures which indicates the influence of particle growth and aggregation. However, close inspection of their Fig. 3 shows that it is possible to see a fractional decrease ($\sim 0.05 \text{ m s}^{-1}$) in the average lidar Doppler velocity at around -16°C . Using the same dataset, Westbrook et al. (2010) investigate the fall speeds of specularly reflecting ice crystals in layer clouds; these are assumed to be planar crystal types, such as plate-like and dendritic crystals. The distribution of fall speeds of specularly reflecting particles shows evidence that instead of systematically increasing with temperature, there is a reduction in particle velocity at approximately -13°C (see Fig. 13 in Westbrook et al., 2010). As these statistics are shown for specularly reflecting crystals, and this temperature is within the dendritic growth layer (DGL), it is reasonable to suggest that the dominant crystal type at this temperature is dendritic. This feature is not discussed by Westbrook et al. (2010), but rather is treated as evidence of the velocity distribution of specularly reflecting crystals being slower and having a weaker variation with temperature compared to the statistics shown for ‘normal’ (i.e. non-specularly reflecting) ice cloud in Westbrook and Illingworth (2009). However, comparisons with results shown in Figs. 15 and 16 shows evidence that the results shown by Westbrook et al. (2010) are in fact in agreement with the suggestion that dendritic crystals, whether pristine dendrites or precipitating particles with dendritic growth, consistently fall more slowly than different crystal types in other temperature regimes.

There have been different explanations in literature for observations of decreased MDV in the DGL. One suggestion is that the presence of a slow-falling secondary ice mode acts to decrease the observed MDV (Schrom and Kumjian, 2016). An alternative interpretation (Zawadzki, 2013) suggests that these changes at -15°C are driven by ascending air motion at that level. However, our observation of multimodal spectra at this temperature over many events seems inconsistent with this idea



as it is not obvious why ascent would be concentrated at that particular temperature. Our data is dominated by frontal clouds formed by large-scale ascent, which occurs over a wide range of temperatures. Another explanation suggests that enhanced
510 depositional growth in the DGL causes latent heat release that is sufficient to increase buoyancy and consequently cause upward air motion (Zawadzki, 2013; Schrom and Kumjian, 2016). von Terzi et al. (2022) test these interpretations by analysing spectral edge velocities and conclude that the reduction in MDV is the result of new particle formation with low fall velocities combined with the presence of a weak updraft likely caused by latent heat release from enhanced depositional growth. Our results instead show evidence that changes in the primary population typically govern this decrease in MDV.

515 4.5 Discussion of mechanisms for multimodality

In Fig. 14, we show clear evidence that there are two temperature regimes in which multimodal spectra are frequently detected. These temperature regimes are located between approximately -8°C and -3°C , where up to 40 % of spectra are multimodal, and between approximately -18°C and -10°C , where up to 20 % of spectra are multimodal. Whilst relatively little research into ice multiplication has focussed on frontal clouds, Mammatt et al. (2026) show evidence from a frontal case study that
520 multimodal particle size distributions (PSDs) at -5°C are likely to be caused by rime splintering. This conclusion was based on analysis of particle shape which showed clear evidence of two distinct particle populations coexisting in the same cloud volume, along with observations of needle crystals which were significantly higher in concentration than the expected ice nuclei concentration (DeMott et al., 2010), and which occurred in conditions with significant liquid water content (LWC). Given that the case studies described in Table 1 were selected to represent similar cloud types (i.e. stratiform frontal clouds), we suggest
525 that rime splintering may also be active at similar temperatures in many or all of the cases analysed here.

The frequent detection of multimodal spectra between -18°C and -10°C is more puzzling. In Figs. 15 and 16, we show evidence that there is a local minimum in the velocity of the primary population in the DGL; we suggest is caused by growth of dendritic branches on particles falling from higher altitudes, which acts to increase their drag and reduce the fall speeds of those particles. One possible explanation for the formation of the secondary mode in this temperature regime is that secondary
530 particles are created by collisions between ice particles. Dendritic branches are thin and one could imagine that they could therefore break away from the rest of the ice particle or shatter into small fragments on impact (Grzegorzczuk et al., 2023, and references therein). Once detached, these tiny fragments will grow from vapour into new ice particles, producing a new population of small, slow-falling secondary particles which grow larger and sediment faster as they evolve and settle through the DGL. These will appear as a slow mode in the Doppler spectra with the velocity of this secondary peak increasing in
535 magnitude as they fall to lower altitudes, consistent with our observations.

Weighing against this interpretation is the observation that the local minimum in Doppler velocity in the DGL is observed systematically in monomodal spectra as well as multimodal spectra. In fact, Fig. 15 shows that this minimum is more pronounced in monomodal cases than in multimodal ones. If dendritic arms are growing on particles precipitating from above in these monomodal cases, why do collisions between them not form secondary particles?

540 An alternative hypothesis is that the secondary production process involves riming, and our data provides some evidence to suggest this is the case. When we examine the velocity of the primary population in multimodal spectra it is systematically



higher than it is in monomodal spectra, which suggests that the processes involved in the formation of the multimodal population are also conducive to increasing the fall velocity of the primary population. Riming is an effective mechanism to increase the fall speed of snowflakes (Garrett and Yuter, 2014; Moisseev et al., 2017). The existing literature on rime splintering is focussed on the temperature window near -5°C , where Hallett and Mossop (1974) report hundreds of secondary ice particles produced per milligram of rime. However, close examination of their Fig. 2 reveals a slower (but non-zero) production rate of a few tens of splinters per milligram of rime at -13.5°C and -15.5°C . If those findings are accurate, then our measurements could potentially be explained by a (relatively slow) rime splintering process in the DGL.

The uncertainty surrounding both the mechanism producing multimodal spectra and mechanism causing the observed decrease in primary population velocity in the DGL demonstrates the importance of further research into the microphysical processes active at these temperatures. In particular, ice multiplication and aggregation processes involving dendritic particles remain poorly understood. For example, if increased drag force against pristine dendritic crystals causes a decrease in velocity, what happens when dendritic crystals aggregate – does the velocity increase due to the increased mass, or does the velocity remain similar or continue to decrease due to increased air resistance? Are the rime splintering or ice-ice fragmentation mechanisms efficient enough at low temperatures in non-turbulent clouds to cause one fifth of all spectra at these temperatures to be multimodal?

The implications of these findings are apparent for NWP, where ice microphysical processes are crudely represented. For example, some models have no parameterisation in place to represent SIP (Wilson and Ballard, 1999; ECMWF, 2024), and those that do are usually focussed on rime splintering (Korolev and Leisner, 2020). Ice microphysical processes such as SIP have significant influences on cloud development and inaccurate representation can cause large errors in forecast process rates (Mammatt et al., 2026), thus demonstrating the importance of continued efforts to better understand these fundamental processes.

5 Conclusions

We have used radar Doppler spectra from 23 case studies to analyse the distribution of multimodal spectra in midlatitude frontal clouds. We have presented a method for detecting multimodal spectra using a peak finding algorithm, which is applied to the case studies. Results from two cases are shown to demonstrate the variability in the selected cases, and to show qualitatively how the spatial distribution of multimodal spectra changes between cases. The results from the peak finding algorithm enable us to quantitatively estimate the distribution of multimodal spectra with temperature for the first time; whilst there is no clear method to quantify the errors caused by inaccurate peak detection due to the unique nature of each Doppler spectrum (Shupe et al., 2004), we believe this to be a conservative estimate based on relatively strict turbulence and peak finding thresholds. We find there are two distinct temperature regimes where multimodal spectra are frequently detected. The first of these is between -3°C and -8°C where up to 40 % of spectra are multimodal, which is consistent with the temperatures which at rime splintering occurs. Indeed, Mammatt et al. (2026) investigate the final case study used in this work (Table 1) in greater detail, and show evidence from aircraft observations that coexisting populations of dendritic crystals and needle crystals are



575 responsible for producing multimodal PSDs, which are likely to produce the multimodal spectra observed. It is reasonable to
assume that the same microphysical processes are active in the majority of cases studies selected for the analysis presented in
this paper, as they were chosen to represent clouds similar to the one analysed in Mammatt et al. (2026). The other temperature
regime where multimodal spectra are frequently observed is between temperatures of -18°C and -10°C , where up to 20 % of
spectra are multimodal. The mechanism responsible for the multimodal spectra detected at this temperature is unclear, but we
580 suggest is likely to be caused by SIP.

The peak finding algorithm also returns the velocity corresponding to the peak spectral reflectivity for each Doppler spec-
trum, from which we produce the vertical profile of peak particle population velocities. These results can be separated into
profiles for monomodal spectra and multimodal spectra, and provide evidence that there is a consistent decrease in particle
velocity at temperatures around -13°C in monomodal spectra; we hypothesise that this is caused by increased drag against
585 particles with open geometry such as those with dendritic growth. The velocity of the primary population in multimodal spec-
tra is higher than that in monomodal spectra, and the decrease in particle velocities at -13°C is much apparent. Similar analysis
can be performed for MDV, which can be separated for monomodal and multimodal spectra. Similarly to the particle velocity,
a minimum in MDV is observed at -13°C in monomodal spectra, and MDV from multimodal spectra is consistently higher
than from monomodal spectra. This suggests that the conditions conducive to forming multimodal spectra are also conducive
590 to growing the primary population. The mechanism behind this is unclear, but may be a result of riming or collisions between
ice particles. As it is not possible to prove the occurrence of microphysical processes such as SIP and riming solely from radar
observations, (Lauber et al., 2021; Luke et al., 2021; Li et al., 2021), the continued uncertainties surrounding the mechanisms
active in frontal stratiform clouds demonstrates the importance of continued research into secondary ice production, especially
at temperatures outside of the rime splintering regime, and processes active in the DGL.

595 *Data availability.* Data are available through the CEDA Archive. Further information about the data and conditions for access are available
at: <https://www.ceda.ac.uk/services/ceda-archive/>.

Author contributions. RMM, CW and KMC contributed to conceptualisation of the study. RMM lead the formal analysis and wrote the
manuscript draft. CW and KM provided project supervision, and review and editing of the manuscript.

Competing interests. The authors declare that they have no conflict of interest.

600 *Acknowledgements.* We acknowledge the efforts of Chris Walden and the staff at the Chilbolton Observatory in the collection of the radar
data presented here. The data collection was supported by NERC grant NE/P012426/1.



References

- Babb, D. M., Verlinde, J., and Rust, B. W.: The Removal of Turbulent Broadening in Radar Doppler Spectra Using Linear Inversion with Double-Sided Constraints, *Journal of Atmospheric and Oceanic Technology*, 17, 1583–1595, [https://doi.org/10.1175/1520-0426\(2000\)017<1583:TROTBI>2.0.CO;2](https://doi.org/10.1175/1520-0426(2000)017<1583:TROTBI>2.0.CO;2), 2000.
- 605
- Billault-Roux, A.-C., Georgakaki, P., Gehring, J., Jaffeux, L., Schwarzenboeck, A., Coutris, P., Nenes, A., and Berne, A.: Distinct secondary ice production processes observed in radar Doppler spectra: insights from a case study, *Atmospheric Chemistry and Physics*, 23, 10207–10234, <https://doi.org/10.5194/acp-23-10207-2023>, 2023.
- Crosier, J., Bower, K. N., Choulaton, T. W., Westbrook, C. D., Connolly, P. J., Cui, Z. Q., Crawford, I. P., Capes, G. L., Coe, H., Dorsey, J. R., Williams, P. I., Illingworth, A. J., Gallagher, M. W., and Blyth, A. M.: Observations of ice multiplication in a weakly convective cell embedded in supercooled mid-level stratus, *Atmospheric Chemistry and Physics*, 11, 257–273, <https://doi.org/10.5194/acp-11-257-2011>, 2011.
- 610
- Crosier, J., Choulaton, T. W., Westbrook, C. D., Blyth, A. M., Bower, K. N., Connolly, P. J., Dearden, C., Gallagher, M. W., Cui, Z., and Nicol, J. C.: Microphysical properties of cold frontal rainbands, *Quarterly Journal of the Royal Meteorological Society*, 140, 1257–1268, <https://doi.org/10.1002/qj.2206>, [_eprint: https://onlinelibrary.wiley.com/doi/pdf/10.1002/qj.2206](https://onlinelibrary.wiley.com/doi/pdf/10.1002/qj.2206), 2014.
- 615
- DeMott, P. J., Prenni, A. J., Liu, X., Kreidenweis, S. M., Petters, M. D., Twohy, C. H., Richardson, M. S., Eidhammer, T., and Rogers, D. C.: Predicting global atmospheric ice nuclei distributions and their impacts on climate, *Proceedings of the National Academy of Sciences*, 107, 11217–11222, <https://doi.org/10.1073/pnas.0910818107>, 2010.
- ECMWF: IFS Documentation CY49R1 - Part IV: Physical Processes, in: IFS Documentation CY49R1, ECMWF, <https://www.ecmwf.int/en/eLibrary/81626-ifs-documentation-cy49r1-part-iv-physical-processes>, 2024.
- 620
- Field, P. R. and Heymsfield, A. J.: Importance of snow to global precipitation, *Geophysical Research Letters*, 42, 9512–9520, <https://doi.org/10.1002/2015GL065497>, [_eprint: https://onlinelibrary.wiley.com/doi/pdf/10.1002/2015GL065497](https://onlinelibrary.wiley.com/doi/pdf/10.1002/2015GL065497), 2015.
- Field, P. R., Hogan, R. J., Brown, P. R. A., Illingworth, A. J., Choulaton, T. W., and Cotton, R. J.: Parametrization of ice-particle size distributions for mid-latitude stratiform cloud, *Quarterly Journal of the Royal Meteorological Society*, 131, 1997–2017, <https://doi.org/10.1256/qj.04.134>, [_eprint: https://rmets.onlinelibrary.wiley.com/doi/pdf/10.1256/qj.04.134](https://rmets.onlinelibrary.wiley.com/doi/pdf/10.1256/qj.04.134), 2005.
- 625
- Field, P. R., Lawson, R. P., Brown, P. R. A., Lloyd, G., Westbrook, C., Moisseev, D., Miltenberger, A., Nenes, A., Blyth, A., Choulaton, T., Connolly, P., Buehl, J., Crosier, J., Cui, Z., Dearden, C., DeMott, P., Flossmann, A., Heymsfield, A., Huang, Y., Kalesse, H., Kanji, Z. A., Korolev, A., Kirchgaessner, A., Lasher-Trapp, S., Leisner, T., McFarquhar, G., Phillips, V., Stith, J., and Sullivan, S.: Secondary Ice Production: Current State of the Science and Recommendations for the Future, *Meteorological Monographs*, 58, 7.1–7.20, <https://doi.org/10.1175/AMSMONOGRAPHS-D-16-0014.1>, 2017.
- 630
- Field, P. R., Hill, A., Shipway, B., Furtado, K., Wilkinson, J., Miltenberger, A., Gordon, H., Grosvenor, D. P., Stevens, R., and Van Weverberg, K.: Implementation of a double moment cloud microphysics scheme in the UK met office regional numerical weather prediction model, *Quarterly Journal of the Royal Meteorological Society*, 149, 703–739, <https://doi.org/10.1002/qj.4414>, [_eprint: https://onlinelibrary.wiley.com/doi/pdf/10.1002/qj.4414](https://onlinelibrary.wiley.com/doi/pdf/10.1002/qj.4414), 2023.
- 635
- Garrett, T. J. and Yuter, S. E.: Observed influence of riming, temperature, and turbulence on the fallspeed of solid precipitation, *Geophysical Research Letters*, 41, 6515–6522, <https://doi.org/10.1002/2014GL061016>, [_eprint: https://onlinelibrary.wiley.com/doi/pdf/10.1002/2014GL061016](https://onlinelibrary.wiley.com/doi/pdf/10.1002/2014GL061016), 2014.



- Grzegorzczak, P., Yadav, S., Zanger, F., Theis, A., Mitra, S. K., Borrmann, S., and Szakáll, M.: Fragmentation of ice particles: laboratory experiments on graupel–graupel and graupel–snowflake collisions, *Atmospheric Chemistry and Physics*, 23, 13 505–13 521, <https://doi.org/10.5194/acp-23-13505-2023>, 2023.
- 640 Hallett, J. and Mossop, S. C.: Production of secondary ice particles during the riming process, *Nature*, 249, 26–28, <https://doi.org/10.1038/249026a0>, 1974.
- Heymsfield, A. J. and Westbrook, C. D.: Advances in the Estimation of Ice Particle Fall Speeds Using Laboratory and Field Measurements, *Journal of the Atmospheric Sciences*, 67, 2469–2482, <https://doi.org/10.1175/2010JAS3379.1>, 2010.
- 645 Heymsfield, A. J., Schmitt, C., Chen, C.-C.-J., Bansemer, A., Gettelman, A., Field, P. R., and Liu, C.: Contributions of the Liquid and Ice Phases to Global Surface Precipitation: Observations and Global Climate Modeling, *Journal of the Atmospheric Sciences*, <https://doi.org/10.1175/JAS-D-19-0352.1>, 2020.
- Hofer, S., Tedstone, A. J., Fettweis, X., and Bamber, J. L.: Cloud microphysics and circulation anomalies control differences in future Greenland melt, *Nature Climate Change*, 9, 523–528, <https://doi.org/10.1038/s41558-019-0507-8>, 2019.
- 650 Illingworth, A. J., Hogan, R. J., O’Connor, E., Bouniol, D., Brooks, M. E., Delanoé, J., Donovan, D. P., Eastment, J. D., Gaussiat, N., Goddard, J. W. F., Haeffelin, M., Baltink, H. K., Krasnov, O. A., Pelon, J., Piriou, J.-M., Protat, A., Russchenberg, H. W. J., Seifert, A., Tompkins, A. M., Van Zadelhoff, G.-J., Vinit, F., Willén, U., Wilson, D. R., and Wrench, C. L.: Cloudnet: Continuous Evaluation of Cloud Profiles in Seven Operational Models Using Ground-Based Observations, *Bulletin of the American Meteorological Society*, 88, 883–898, <https://doi.org/10.1175/BAMS-88-6-883>, 2007.
- 655 Illingworth, A. J., Barker, H. W., Beljaars, A., Ceccaldi, M., Chepfer, H., Clerbaux, N., Cole, J., Delanoë, J., Domenech, C., Donovan, D. P., Fukuda, S., Hiraoka, M., Hogan, R. J., Huenerbein, A., Kollias, P., Kubota, T., Nakajima, T., Nakajima, T. Y., Nishizawa, T., Ohno, Y., Okamoto, H., Oki, R., Sato, K., Satoh, M., Shephard, M. W., Velázquez-Blázquez, A., Wandinger, U., Wehr, T., and Zadelhoff, G.-J. v.: The EarthCARE Satellite: The Next Step Forward in Global Measurements of Clouds, Aerosols, Precipitation, and Radiation, *Bulletin of the American Meteorological Society*, <https://doi.org/10.1175/BAMS-D-12-00227.1>, 2015.
- 660 Kalesse, H., Szyrmer, W., Kneifel, S., Kollias, P., and Luke, E.: Fingerprints of a riming event on cloud radar Doppler spectra: observations and modeling, *Atmospheric Chemistry and Physics*, 16, 2997–3012, <https://doi.org/10.5194/acp-16-2997-2016>, 2016.
- Keinert, A., Spannagel, D., Leisner, T., and Kiselev, A.: Secondary Ice Production upon Freezing of Freely Falling Drizzle Droplets, *Journal of the Atmospheric Sciences*, 77, 2959–2967, <https://doi.org/10.1175/JAS-D-20-0081.1>, 2020.
- Keppas, S. C., Crosier, J., Choulaton, T. W., and Bower, K. N.: Ice lollies: An ice particle generated in super-cooled conveyor belts, *Geophysical Research Letters*, 44, 5222–5230, <https://doi.org/10.1002/2017GL073441>, [_eprint: https://onlinelibrary.wiley.com/doi/pdf/10.1002/2017GL073441](https://onlinelibrary.wiley.com/doi/pdf/10.1002/2017GL073441), 2017.
- 665 Kneifel, S. and Moisseev, D.: Long-Term Statistics of Riming in Nonconvective Clouds Derived from Ground-Based Doppler Cloud Radar Observations, *Journal of the Atmospheric Sciences*, <https://doi.org/10.1175/JAS-D-20-0007.1>, 2020.
- Kneifel, S., Kollias, P., Battaglia, A., Leinonen, J., Maahn, M., Kalesse, H., and Tridon, F.: First observations of triple-frequency radar Doppler spectra in snowfall: Interpretation and applications, *Geophysical Research Letters*, 43, 2225–2233, <https://doi.org/10.1002/2015GL067618>, [_eprint: https://agupubs.onlinelibrary.wiley.com/doi/pdf/10.1002/2015GL067618](https://agupubs.onlinelibrary.wiley.com/doi/pdf/10.1002/2015GL067618), 2016.
- 670 Kollias, P., Albrecht, B. A., and Marks, F.: Why Mie?, *Bulletin of the American Meteorological Society*, <https://doi.org/10.1175/BAMS-83-10-1471>, 2002.
- Korolev, A. and Leisner, T.: Review of experimental studies of secondary ice production, *Atmospheric Chemistry and Physics*, 20, 11 767–11 797, <https://doi.org/10.5194/acp-20-11767-2020>, 2020.
- 675



- Korolev, A., DeMott, P. J., Heckman, I., Wolde, M., Williams, E., Smalley, D. J., and Donovan, M. F.: Observation of secondary ice production in clouds at low temperatures, *Atmospheric Chemistry and Physics*, 22, 13 103–13 113, <https://doi.org/10.5194/acp-22-13103-2022>, 2022.
- Lauber, A., Kiselev, A., Pander, T., Handmann, P., and Leisner, T.: Secondary Ice Formation during Freezing of Levitated Droplets, *Journal of the Atmospheric Sciences*, 75, 2815–2826, <https://doi.org/10.1175/JAS-D-18-0052.1>, 2018.
- 680 Lauber, A., Henneberger, J., Mignani, C., Ramelli, F., Pasquier, J. T., Wieder, J., Hervo, M., and Lohmann, U.: Continuous secondary-ice production initiated by updrafts through the melting layer in mountainous regions, *Atmospheric Chemistry and Physics*, 21, 3855–3870, <https://doi.org/10.5194/acp-21-3855-2021>, 2021.
- Li, H., Korolev, A., and Moisseev, D.: Supercooled liquid water and secondary ice production in Kelvin–Helmholtz instability as revealed by radar Doppler spectra observations, *Atmospheric Chemistry and Physics*, 21, 13 593–13 608, <https://doi.org/10.5194/acp-21-13593-2021>,
685 2021.
- Lloyd, G., Dearden, C., Choullarton, T. W., Crosier, J., and Bower, K. N.: Observations of the Origin and Distribution of Ice in Cold, Warm, and Occluded Frontal Systems during the DIAMET Campaign, *Monthly Weather Review*, <https://doi.org/10.1175/MWR-D-13-00396.1>, 2014.
- Locatelli, J. D. and Hobbs, P. V.: Fall speeds and masses of solid precipitation particles, *Journal of Geophysical Research* (1896-1977), 79, 2185–2197, <https://doi.org/10.1029/JC079i015p02185>, _eprint: <https://onlinelibrary.wiley.com/doi/pdf/10.1029/JC079i015p02185>, 1974.
- 690 Lohmann, U. and Feichter, J.: Global indirect aerosol effects: a review, *Atmospheric Chemistry and Physics*, 5, 715–737, <https://doi.org/10.5194/acp-5-715-2005>, 2005.
- Luke, E. P. and Kollias, P.: Separating Cloud and Drizzle Radar Moments during Precipitation Onset Using Doppler Spectra, *Journal of Atmospheric and Oceanic Technology*, <https://doi.org/10.1175/JTECH-D-11-00195.1>, 2013.
- 695 Luke, E. P., Yang, F., Kollias, P., Vogelmann, A. M., and Maahn, M.: New insights into ice multiplication using remote-sensing observations of slightly supercooled mixed-phase clouds in the Arctic, *Proceedings of the National Academy of Sciences*, 118, e2021387 118, <https://doi.org/10.1073/pnas.2021387118>, 2021.
- Mammatt, R. M., Westbrook, C. D., Crosier, J., and McCusker, K.: Evaluating the realism of double moment parameterised particle size distributions in a midlatitude frontal ice cloud with complex microphysics, *Quarterly Journal of the Royal Meteorological Society*, n/a, e70 172, <https://doi.org/10.1002/qj.70172>, _eprint: <https://rmets.onlinelibrary.wiley.com/doi/pdf/10.1002/qj.70172>, 2026.
- 700 Matrosov, S. Y.: Attenuation-Based Estimates of Rainfall Rates Aloft with Vertically Pointing Ka-Band Radars, *Journal of Atmospheric and Oceanic Technology*, <https://doi.org/10.1175/JTECH-1677.1>, 2005.
- Moisseev, D., von Lerber, A., and Tiira, J.: Quantifying the effect of riming on snowfall using ground-based observations, *Journal of Geophysical Research: Atmospheres*, 122, 4019–4037, <https://doi.org/10.1002/2016JD026272>, _eprint: <https://agupubs.onlinelibrary.wiley.com/doi/pdf/10.1002/2016JD026272>, 2017.
- 705 Mosimann, L.: An improved method for determining the degree of snow crystal riming by vertical Doppler radar, *Atmospheric Research*, 37, 305–323, [https://doi.org/10.1016/0169-8095\(94\)00050-N](https://doi.org/10.1016/0169-8095(94)00050-N), 1995.
- Mülmenstädt, J., Salzmann, M., Kay, J. E., Zelinka, M. D., Ma, P.-L., Nam, C., Kretschmar, J., Hörnig, S., and Quaas, J.: An underestimated negative cloud feedback from cloud lifetime changes, *Nature Climate Change*, 11, 508–513, <https://doi.org/10.1038/s41558-021-01038-1>,
710 2021.
- Norbury, J. R. and White, W. J.: A rapid-response rain gauge, *Journal of Physics E: Scientific Instruments*, 4, 601, <https://doi.org/10.1088/0022-3735/4/8/013>, 1971.



- O'Connor, E. J., Hogan, R. J., and Illingworth, A. J.: Retrieving Stratocumulus Drizzle Parameters Using Doppler Radar and Lidar, *Journal of Applied Meteorology and Climatology*, <https://doi.org/10.1175/JAM-2181.1>, 2005.
- 715 Pasquier, J. T., Henneberger, J., Korolev, A., Ramelli, F., Wieder, J., Lauber, A., Li, G., David, R. O., Carlsen, T., Gierens, R., Maturilli, M., and Lohmann, U.: Understanding the History of Two Complex Ice Crystal Habits Deduced From a Holographic Imager, *Geophysical Research Letters*, 50, e2022GL100247, <https://doi.org/10.1029/2022GL100247>, _eprint: <https://onlinelibrary.wiley.com/doi/pdf/10.1029/2022GL100247>, 2023.
- Phillips, V. T. J., Yano, J.-I., and Khain, A.: Ice Multiplication by Breakup in Ice–Ice Collisions. Part I: Theoretical Formulation, *Journal of the Atmospheric Sciences*, 74, <https://doi.org/10.1175/JAS-D-16-0224.1>, 2017.
- 720 Phillips, V. T. J., Patade, S., Gutierrez, J., and Bansemer, A.: Secondary Ice Production by Fragmentation of Freezing Drops: Formulation and Theory, *Journal of the Atmospheric Sciences*, 75, <https://doi.org/10.1175/JAS-D-17-0190.1>, 2018.
- Protat, A. and Williams, C. R.: The Accuracy of Radar Estimates of Ice Terminal Fall Speed from Vertically Pointing Doppler Radar Measurements, *Journal of Applied Meteorology and Climatology*, <https://doi.org/10.1175/JAMC-D-10-05031.1>, 2011.
- 725 Radenz, M., Bühl, J., Seifert, P., Griesche, H., and Engelmann, R.: peakTree: a framework for structure-preserving radar Doppler spectra analysis, *Atmospheric Measurement Techniques*, 12, 4813–4828, <https://doi.org/10.5194/amt-12-4813-2019>, 2019.
- Schrom, R. S. and Kumjian, M. R.: Connecting Microphysical Processes in Colorado Winter Storms with Vertical Profiles of Radar Observations, *Journal of Applied Meteorology and Climatology*, 55, 1771–1787, <https://doi.org/10.1175/JAMC-D-15-0338.1>, 2016.
- Seidel, J. S., Kiselev, A. A., Keinert, A., Stratmann, F., Leisner, T., and Hartmann, S.: Secondary ice production – no evidence of efficient rime-splintering mechanism, *Atmospheric Chemistry and Physics*, 24, 5247–5263, <https://doi.org/10.5194/acp-24-5247-2024>, 2024.
- 730 Sherwood, S. C., Webb, M. J., Annan, J. D., Armour, K. C., Forster, P. M., Hargreaves, J. C., Hegerl, G., Klein, S. A., Marvel, K. D., Rohling, E. J., Watanabe, M., Andrews, T., Braconnot, P., Bretherton, C. S., Foster, G. L., Hausfather, Z., von der Heydt, A. S., Knutti, R., Mauritsen, T., Norris, J. R., Proistosescu, C., Rugenstein, M., Schmidt, G. A., Tokarska, K. B., and Zelinka, M. D.: An Assessment of Earth’s Climate Sensitivity Using Multiple Lines of Evidence, *Reviews of Geophysics*, 58, e2019RG000678, <https://doi.org/10.1029/2019RG000678>, _eprint: <https://onlinelibrary.wiley.com/doi/pdf/10.1029/2019RG000678>, 2020.
- 735 Shupe, M. D., Kollias, P., Matrosov, S. Y., and Schneider, T. L.: Deriving Mixed-Phase Cloud Properties from Doppler Radar Spectra, *Journal of Atmospheric and Oceanic Technology*, https://journals.ametsoc.org/view/journals/atot/21/4/1520-0426_2004_021_0660_dmcpfd_2_0_co_2.xml, 2004.
- Sun, Z. and Shine, K. P.: Studies of the radiative properties of ice and mixed-phase clouds, *Quarterly Journal of the Royal Meteorological Society*, 120, 111–137, <https://doi.org/10.1002/qj.49712051508>, _eprint: <https://rmets.onlinelibrary.wiley.com/doi/pdf/10.1002/qj.49712051508>, 1994.
- 740 Vardiman, L.: The Generation of Secondary Ice Particles in Clouds by Crystal–Crystal Collision, *Journal of the Atmospheric Sciences*, https://journals.ametsoc.org/view/journals/atsc/35/11/1520-0469_1978_035_2168_tgosip_2_0_co_2.xml, 1978.
- Virtanen, P., Gommers, R., Oliphant, T. E., Haberland, M., Reddy, T., Cournapeau, D., Burovski, E., Peterson, P., Weckesser, W., Bright, J., van der Walt, S. J., Brett, M., Wilson, J., Millman, K. J., Mayorov, N., Nelson, A. R. J., Jones, E., Kern, R., Larson, E., Carey, C. J., Polat, I., Feng, Y., Moore, E. W., VanderPlas, J., Laxalde, D., Perktold, J., Cimrman, R., Henriksen, I., Quintero, E. A., Harris, C. R., Archibald, A. M., Ribeiro, A. H., Pedregosa, F., and van Mulbregt, P.: SciPy 1.0: fundamental algorithms for scientific computing in Python, *Nature Methods*, 17, 261–272, <https://doi.org/10.1038/s41592-019-0686-2>, 2020.



- Vogl, T., Radenz, M., Ramelli, F., Gierens, R., and Kalesse-Los, H.: PEAKO and peakTree: tools for detecting and interpreting peaks in cloud radar Doppler spectra – capabilities and limitations, *Atmospheric Measurement Techniques*, 17, 6547–6568, <https://doi.org/10.5194/amt-17-6547-2024>, 2024.
- von Terzi, L., Dias Neto, J., Ori, D., Myagkov, A., and Kneifel, S.: Ice microphysical processes in the dendritic growth layer: a statistical analysis combining multi-frequency and polarimetric Doppler cloud radar observations, *Atmospheric Chemistry and Physics*, 22, 11 795–11 821, <https://doi.org/10.5194/acp-22-11795-2022>, 2022.
- 755 Walden, C.: UKRI Copernicus. ACTRIS Cloud remote sensing data centre unit (CLU), <https://hdl.handle.net/21.12132/3.c3e825b4aa71435c>, 2026.
- Wedi, N., Bauer, P., Deconinck, W., Diamantakis, M., Hamrud, M., Kuehnlein, C., Malardel, S., Mogensen, K., Mozdzyński, G., and Smolarkiewicz, P.: The modelling infrastructure of the Integrated Forecasting System: Recent advances and future challenges, <https://doi.org/10.21957/thtpwp67e>, issue: 760 Publication Title: ECMWF Technical Memoranda, 2015.
- 760 Wehr, T., Kubota, T., Tzeremes, G., Wallace, K., Nakatsuka, H., Ohno, Y., Koopman, R., Rusli, S., Kikuchi, M., Eisinger, M., Tanaka, T., Taga, M., Deghaye, P., Tomita, E., and Bernaerts, D.: The EarthCARE mission – science and system overview, *Atmospheric Measurement Techniques*, 16, 3581–3608, <https://doi.org/10.5194/amt-16-3581-2023>, 2023.
- Westbrook, C. D. and Illingworth, A. J.: Testing the influence of small crystals on ice size spectra using Doppler lidar observations, *Geophysical Research Letters*, 36, <https://doi.org/10.1029/2009GL038186>, <https://onlinelibrary.wiley.com/doi/pdf/10.1029/2009GL038186>, 2009.
- 765 Westbrook, C. D., Illingworth, A. J., O’Connor, E. J., and Hogan, R. J.: Doppler lidar measurements of oriented planar ice crystals falling from supercooled and glaciated layer clouds, *Quarterly Journal of the Royal Meteorological Society*, 136, 260–276, <https://doi.org/10.1002/qj.528>, [eprint: https://onlinelibrary.wiley.com/doi/pdf/10.1002/qj.528](https://onlinelibrary.wiley.com/doi/pdf/10.1002/qj.528), 2010.
- Wiener, V., Roussel, M.-L., Genthon, C., Vignon, E., Grazioli, J., and Berne, A.: A 7-year record of vertical profiles of radar measurements and precipitation estimates at Dumont d’Urville, Adélie Land, East Antarctica, *Earth System Science Data*, 16, 821–836, <https://doi.org/10.5194/essd-16-821-2024>, 2024.
- 770 Wildeman, S., Sterl, S., Sun, C., and Lohse, D.: Fast Dynamics of Water Droplets Freezing from the Outside In, *Physical Review Letters*, 118, 084 101, <https://doi.org/10.1103/PhysRevLett.118.084101>, 2017.
- Wilson, D. R. and Ballard, S. P.: A microphysically based precipitation scheme for the UK meteorological office unified model, *Quarterly Journal of the Royal Meteorological Society*, 125, 1607–1636, <https://doi.org/10.1002/qj.49712555707>, [eprint: https://onlinelibrary.wiley.com/doi/pdf/10.1002/qj.49712555707](https://onlinelibrary.wiley.com/doi/pdf/10.1002/qj.49712555707), 1999.
- 775 Yano, J.-I. and Phillips, V. T. J.: Ice–Ice Collisions: An Ice Multiplication Process in Atmospheric Clouds, *Journal of the Atmospheric Sciences*, 68, 322–333, <https://doi.org/10.1175/2010JAS3607.1>, 2011.
- Yano, J.-I., Phillips, V. T. J., and Kanawade, V.: Explosive ice multiplication by mechanical break-up in ice–ice collisions: a dynamical system-based study, *Quarterly Journal of the Royal Meteorological Society*, 142, 867–879, <https://doi.org/10.1002/qj.2687>, [eprint: https://onlinelibrary.wiley.com/doi/pdf/10.1002/qj.2687](https://onlinelibrary.wiley.com/doi/pdf/10.1002/qj.2687), 2016.
- 780 Zawadzki, I.: Observations of snow growth by a vertically pointing radar, <https://ams.confex.com/ams/36Radar/webprogram/Paper229071.html>, 2013.
- Zawadzki, I., Fabry, F., and Szyrmer, W.: Observations of supercooled water and secondary ice generation by a vertically pointing X-band Doppler radar, *Atmospheric Research*, 59-60, 343–359, [https://doi.org/10.1016/S0169-8095\(01\)00124-7](https://doi.org/10.1016/S0169-8095(01)00124-7), 2001.
- 785

<https://doi.org/10.5194/egusphere-2026-2928>

Preprint. Discussion started: 3 June 2026

© Author(s) 2026. CC BY 4.0 License.



Zhang, W., Shi, X., and Lu, C.: Impacts of the ice-particle size distribution shape parameter on climate simulations with the Community Atmosphere Model Version 6 (CAM6), *Geoscientific Model Development*, 15, 7751–7766, <https://doi.org/10.5194/gmd-15-7751-2022>, 2022.

790 Zikmunda, J. and Vali, G.: Fall Patterns and Fall Velocities of Rimed Ice Crystals, *Journal of the Atmospheric Sciences*, https://journals.ametsoc.org/view/journals/atsc/29/7/1520-0469_1972_029_1334_fpafvo_2_0_co_2.xml, 1972.

Zängl, G., Reinert, D., Rípodas, P., and Baldauf, M.: The ICON (ICOsahedral Non-hydrostatic) modelling framework of DWD and MPI-M: Description of the non-hydrostatic dynamical core, *Quarterly Journal of the Royal Meteorological Society*, 141, 563–579, <https://doi.org/10.1002/qj.2378>, [_eprint: https://rmets.onlinelibrary.wiley.com/doi/pdf/10.1002/qj.2378](https://rmets.onlinelibrary.wiley.com/doi/pdf/10.1002/qj.2378), 2015.